UNIVERSITÄT BONN
Physikalisches Institut

Gas Electron Multipliers: Development of large area GEMs and spherical GEMs

Serge Duarte Pinto

Gaseous radiation detectors have been a crucial part of high-energy physics instrumentation since the 1960s, when the first multiwire proportional counters were built. In the 1990s the first micropattern gas detectors (MPGDs) saw the light; with sub-millimeter feature sizes these novel detectors were faster and more accurate than their predecessors. The gas electron multiplier (GEM) is one of the most successful of these technologies. It is a charge multiplication structure made from a copper clad polymer foil, pierced with a regular and dense pattern of holes. I will describe the properties and the application of GEMs and GEM detectors, and the research and development I have done on this technology. Two of the main objectives were the development of large area GEMs (~ m^2) for particle physics experiments and GEMs with a spherical shape for x-ray or neutron diffraction detectors. Both have been realized, and the new techniques involved are finding their way to applications in research and industry.

Physikalisches Institut
der Universität Bonn
Nußallee 12
D-53115 Bonn

BONN-IR-2011-09
August 2011
ISSN-0172-8741

UNIVERSITÄT BONN
Physikalisches Institut

Gas Electron Multipliers: Development of large area GEMs and spherical GEMs

Serge Duarte Pinto

Dieser Forschungsbericht wurde als Dissertation von der
Mathematisch-Naturwissenschaftlichen-Fakultät der Universität Bonn
angenommen und ist auf der ULB Bonn
http://hss.ulb.uni-bonn.de/diss_online elektronisch publiziert.

Erscheinungsjahr: 2011

Referent: Prof. Ian Brock
Koreferent: Prof. Klaus Desch

Angenommen am: August 2011
Tag der Promotion: 13 July 2011

Introduction

The work presented in this thesis was done between July 2007 and September 2010, when I was enrolled in the CERN *Doctoral Student Programme*. During this period Leszek Ropelewski (CERN) has been supervising my work, while I updated Ian Brock in weekly phone meetings on the progress made. In this period I have done research and development on micropattern gaseous detectors (MPGDs), specifically on the gas electron multiplier (GEM).

Besides the technical work on GEM technology, I have been active in the R&D collaboration for micropattern gas detectors introduced in the first chapter: RD51. As a convener of one of the working groups I organized activities and collaboration meetings, and I came in contact with many groups around the world. This introduced me to all the techniques, technologies and applications described in chapter one. In this chapter I describe briefly the principles and history of gaseous detectors, and give an overview of existing technologies and the aspects of development. I have not been directly involved in any of the developments described in the first chapter, and the publications of the original works are cited.

In the course of my work I have gained a lot of hands-on experience with the methods and techniques for making GEM detectors and testing them. This is the subject of the second chapter. I first discuss four applications of GEMs in high-energy physics experiments. For these applications much of the pioneering work on assembly and operation of GEM-based detectors was done, and many of the methods developed by them are now common practice. The following sections are about the design, assembly and testing of GEM detectors, and reflect my own experience with developing small and large prototypes and testing them in the lab and a test beam.

Chapter three is about the development of large area GEMs. This was the project assigned to me when I started as a doctoral student. Until then, the largest existing GEMs had an active area of 31×31 cm^2, and it was generally agreed that it was not feasible to make GEMs much larger. I developed techniques that eliminated limits to how large GEMs could be manufactured, and techniques that accommodated these large sizes during handling, assembly and operation. Based on these techniques I built a prototype detector with an active area of 66×66 cm^2, which I tested successfully. The project received much attention, and many groups around the world are currently using the methods and techniques I developed. The technique that makes it possible to manufacture such large GEM foils, the *single-mask technique*, is now patented worldwide. [51].

The last chapter is about a project that started more recently, with the objective to make spherically shaped GEMs. I explain why for detection of neutral particles a spherical shape can be crucial for eliminating the *parallax error*. The idea to do this was already raised by Fabio Sauli in the original GEM patent [50], but it was never realized. A company interested in making such intrinsically parallax-free x-ray detectors (Bruker AXS) was willing to finance the R&D necessary to make spherical GEMs. I made a first assembly of a spherical GEM with peripheral components to support and operate it, and showed that it works. Although this work was received enthusiastically at the conferences where it was presented (it was awarded *Student Paper Prizes* at the 2009 and 2010 IEEE Nuclear Science Symposia), it is so far not yet adopted by Bruker.

I have greatly enjoyed these years doing R&D, and I have learnt a lot. I saw how development projects are set up, and what is involved. I learned how efforts and resources are spent, and when to stop if things do not look so promising anymore. And I have come to appreciate the value of collaboration with a network of people doing similar research; being able to discuss ideas and exchange experience. I hope my enthusiasm for R&D and particularly for gas detectors is reflected by this thesis.

Contents

Chapter One

INTRODUCTION TO GAS DETECTORS

In this chapter the principles of gaseous radiation detectors will be introduced. The working principle of all gas detectors is similar: radiation causes ionization in the gas, electrons and ions drift apart in an electric field, and the electrons create further electron-ion pairs in an avalanche process in a region with a strong electrostatic field.

Gaseous detectors differ in how this strong field region is created; many examples will be given to illustrate this. After a short historical introduction to micropattern gas detectors (MPGDs), a few production techniques will be introduced that made it possible to make MPGDs. An overview of detector technologies and their respective merits and applications will be given. Finally, an R&D collaboration for micropattern gas detectors is introduced which plays a key role in the development of these technologies.

1.1 Principles of gaseous detectors

1.1.1 Ionization

Charged particles

Fast charged particles traversing matter lose a fraction of their energy by electromagnetic interactions, thereby causing ionization. The mean energy lost per unit of path length per unit of density of absorber (also called the *stopping power* of the absorber) is well described by the *Bethe equation* [1]:

$$-\left\langle \frac{dE}{dx} \right\rangle = Kz^2 \frac{Z}{A} \frac{1}{\beta^2} \left[\frac{1}{2} \ln \frac{2m_e c^2 \beta^2 \gamma^2 T_{\max}}{I^2} - \beta^2 - \frac{\delta(\beta\gamma)}{2} \right]. \qquad (1.1)$$

Here, $\beta = v/c$ and $\gamma = 1/\sqrt{1-\beta^2}$ as usual, Z and A are the atomic number and atomic mass of the absorber, z is the charge state of the fast particle, $m_e c^2$ is the electron mass (0.511 MeV), I is the mean excitation energy [2], $T_{\max} = 2m_e c^2 \beta^2 \gamma^2$ is the maximum energy loss in a single collision, K is a constant, and $\delta(\beta\gamma)$ is a density correction that is only important in gaseous media and at high energies. The stopping power is usually plotted as a function of $\beta\gamma (= p/Mc)$, as in figure 1.1 for argon. It has a minimum around $\beta\gamma = 3.5$,

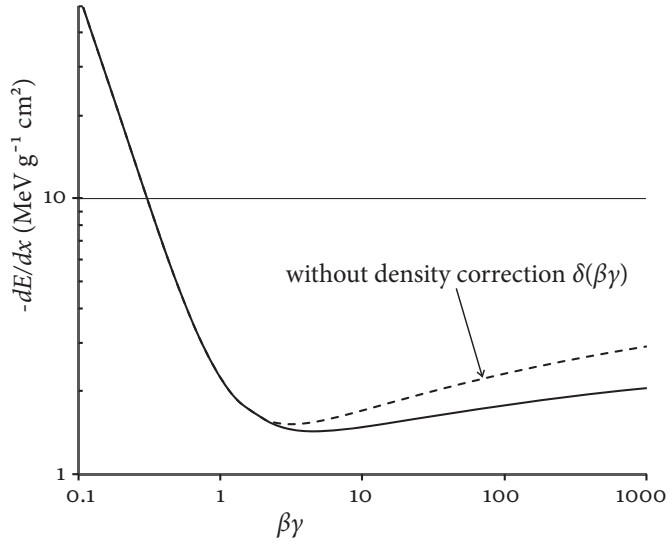

Figure 1.1 — Energy loss of singly charged particles in argon gas, according to the Bethe equation (1.1).

particles with such velocities are therefore called *minimum ionizing particles* (MIPs). Stopping powers of other materials are very similar.

The electrons liberated by interactions of the fast particle with the gas molecules constitute the *primary ionization*. Further ionization is caused by collisions of primary electrons with molecules and by various modes of relaxation of primary excitations; this is called *secondary ionization*. One important de-excitation mechanism leading to ionization is the *Penning transfer*, which occurs when one component of the gas mixture has an excitation energy greater than the ionization potential of another component. Excited molecules from the first component can then ionize the other component, with a probability that depends on the temperature and density.

Most of the charge along a track is from secondary ionization. The range of primary and secondary electrons in a gas at NTP is typically (much) shorter than a millimeter. On the other hand, the average distance between primary ionizations from a relativistic particle is typically a few millimeters. This gives rise to the characteristic charge deposition pattern as an irregular chain of so-called *clusters*, see figure 1.2.

Photons & neutrons

Gaseous detectors can also be used for detection of neutral particles like photons (x-ray or UV) or neutrons. Soft x-rays (up to ~ 12 keV) and thermal neutrons (~ 26 meV) are often used for structural analysis of condensed matter, as their wavelengths are of the order of magnitude of interatomic distances (~

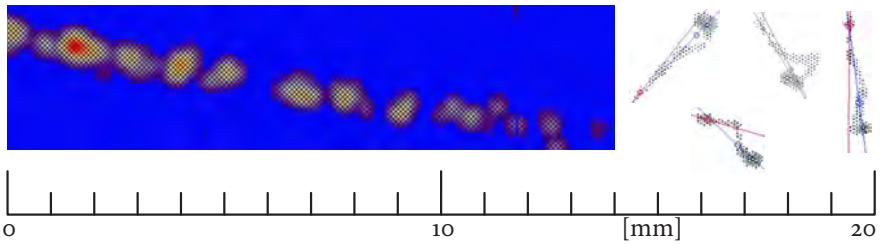

Figure 1.2 — Left (blue background): ionization in clusters along a track, as observed by a highly granular time projection chamber (TPC) with an Ar/CO_2 (70/30 %) gas mixture [4]. Right: 5.4 keV x-ray conversions in an Ne/DME (dimethyl ether) 80/20% gas mixture. Measurements are from a GEM pixel detector [5]. The reconstruction is indicated, marking the conversion point (✙) and the direction of emission of the photoelectron.

1 Å). Large area UV photodetectors are needed for many Cherenkov detectors used in particle physics. As neutral particles do not lose energy in many ionizing interactions along their path like charged particles do, detection depends on a *conversion interaction* which liberates one or more charged particles. In the case of photons this happens by the photoelectric effect. A UV photon yields (with a certain quantum efficiency) a single photoelectron from a solid photoconverter layer or from a component of the gas mixture. Soft x-ray photons (up to ~ 12 keV) liberate a primary photoelectron from the gas, with energy $E = h\nu - \epsilon$, where ϵ is the ionization energy of the gas atom. This energy is lost in collisions with gas molecules, and in total a few hundred electron-ion pairs are thus created. Figure 1.2 includes also some of these conversion events. The heavier noble gases have the highest cross-sections for x-ray absorption, therefore krypton and xenon are frequently used in x-ray detectors. Thermal neutrons (few tens of meV) can be converted by a nuclear reaction with special isotopes of light elements, either in a solid foil or film or as a component of the gas mixture. This reaction yields an ion and a proton or α-particle. Both particles are strongly ionizing: ~ 2 MeV α-particles and 0.57 MeV protons have $\beta\gamma \approx 0.03$, with a mean energy loss more than 100 times higher than MIPs. See table 1.1 for reactions and cross-sections of most commonly used isotopes.

1.1.2 *Drift & diffusion*

The charge from primary and secondary ionizations drifts apart in an electric field of few hundred up to few thousand V/cm. The ions thus recombine at the cathode, while the electrons are transferred to the amplification region.

Table 1.1 — Absorption cross-sections for thermal neutrons (300 K; 26 meV) of a few isotopes, and their conversion reactions. [6]

Isotope	σ(barn)	Reaction
^{3}He	$5.33 \cdot 10^{3}$	$^{3}\mathrm{He} + \mathrm{n} \rightarrow {}^{3}\mathrm{H}(0.19\mathrm{MeV}) + \mathrm{p}(0.57\mathrm{MeV})$
^{6}Li	$9.45 \cdot 10^{2}$	$^{6}\mathrm{Li} + \mathrm{n} \rightarrow {}^{3}\mathrm{H}(2.74\mathrm{MeV}) + \alpha(2.05\mathrm{MeV})$
^{10}B	$4.01 \cdot 10^{3}$	$^{10}\mathrm{B} + \mathrm{n} \rightarrow {}^{7}\mathrm{Li}(0.83\mathrm{MeV}) + \alpha(1.47\mathrm{MeV})$

The drift velocity depends on gas mixture and reduced drift field (defined as the ratio of electric field to pressure, E/p), and is normally a few cm/µs for electrons, and about a thousand times slower for ions. At a microscopic scale, a constant drift velocity is the consequence of many elastic collisions with gas molecules, for which the dynamics are different between electrons and ions. The fractional loss of kinetic energy in an elastic collision is proportional to the mass ratio of the colliding bodies, which for electrons is $\sim 10^{-4}$ and for ions ~ 1. Consequently, ions are almost stopped by each collision, while electrons are scattered isotropically. This causes a significant diffusion of drifting electrons, whereas ions drift nearly perfectly along the electric field. The *diffusion width* of an electron cloud drifting from a point-like origin is defined as the RMS of its transverse lateral distribution:

$$\sigma_x = \sqrt{\frac{2DL}{\mu E}}. \tag{1.2}$$

Here L is the drift length, D is the *diffusion coefficient* and μ is the *electron mobility*; the latter two are properties of gas composition and conditions, D also depends on the magnetic field. Electron diffusion is found to be not entirely isotropic [7], longitudinal diffusion is generally smaller than transverse diffusion.

Magnetic field

The presence of a magnetic field influences drift and diffusion. A magnetic field perpendicular to the electric field, as we find in a transverse tracking station inside the solenoidal magnet of an experiment, introduces a *Lorentz angle* in the drift of electrons. In case the magnetic field is parallel to the electric field, like in a TPC, the transverse diffusion of electrons is suppressed allowing a good spatial resolution even for drift lengths of $\sim$ 1 m. This diffusion suppression is a consequence of the bending of the transverse motion of electrons, thereby reducing their excursion. The longitudinal component of the velocity is not affected, as it is parallel to the magnetic field.

1.1.3 *Amplification*

If the electric field is strong enough ($\gtrapprox$ 10 kV/cm/atm, depending on gas components and density), the drifting electrons gain sufficient kinetic energy between collisions with gas molecules for further ionization. Thus an avalanche develops exponentially, as long as the field is above this multiplication threshold. This process is described by the *first Townsend coefficient* α, which depends on E and the gas composition and density. The increase of the number of electrons N along a path s is expressed as

$$\mathrm{d}N = N\alpha \mathrm{d}s. \tag{1.3}$$

To calculate the gas gain of a certain amplification structure, the above expression must be integrated over the trajectory of a drifting electron:

$$\frac{N}{N_0} = \exp \int_a^b \alpha \mathrm{d}s. \tag{1.4}$$

The boundaries a, b need to cover only the region where the field is sufficiently strong, $\alpha = 0$ elsewhere. Penning transfers, mentioned above, also play an important role in the multiplication mechanism and can increase the gain by an order of magnitude.

Photons

An avalanche also produces photons, usually in similar quantities to electron-ion pairs. A few of these photons may have sufficient energy to cause ionization, either in the gas or on an electrode. If such energetic photons have a range greater than the size of the avalanche, so-called *afterpulses* may occur (by photoelectric effect on the nearest electrode), or the high voltage in the chamber may break down completely (by ionization of gas molecules). To avoid such unstable behavior, the range of UV photons is usually reduced by a so-called *quencher* admixture to the active gas. This is a molecular component, often a hydrocarbon or CO_2, that has a high photo-absorption coefficient due to the molecules' many rotational and translational degrees of freedom.

1.1.4 *Signal induction*

All the moving charges, both electrons and ions, induce currents on the electrodes in the chamber. If an electrode is connected to a charge sensitive amplifier, these induced charges can be read out as electrical signals.

Ramo's theorem [8] describes the current induced on electrode n by the movement of charge q over the path $\mathbf{x}(t)$ with drift velocity $\mathbf{v}(t)$:

$$\mathbf{I}_n^{\mathrm{ind}}(t) = -q\mathbf{E}_n\left[\mathbf{x}(t)\right] \cdot \mathbf{v}(t). \tag{1.5}$$

Here $\mathbf{E}_n$ is the so-called *weighting field* of electrode n, defined as the field obtained by applying a potential of 1 V to that electrode while grounding all other electrodes. Equation 1.5 is exact in case all electrodes are grounded. If some electrodes are connected to ground via some sort of impedance network, a correction term must be added to describe the capacitive coupling of the voltage fluctuations on these electrodes to electrode n [9].

1.2 History and properties of MPGDs

For several decades the most common way to generate a gas amplification field was using thin wires, either one or many, where close to the wire the field strength is inversely proportional to the distance to the wire. This is illustrated in figure 1.3, the first two pictures. The avalanche takes place few tens of microns from the wire, and the electrons are collected immediately. The ions drift back all the way to the cathode; the signals from proportional wires are therefore almost entirely based on the movement of ions.

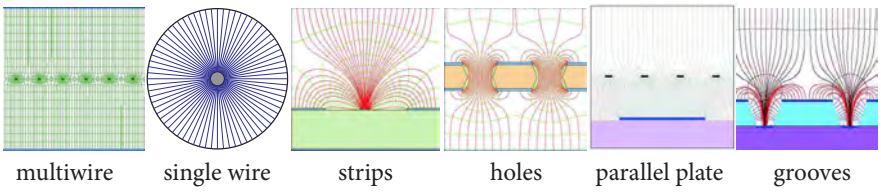

Figure 1.3 — Computed electric field profiles for various micropattern technologies.

In recent years, many planar structures have emerged that generate an enhanced field region in various ways. Several examples are shown in figure 1.3 and many more have been developed. Common feature among all these structures is a narrow amplification gap of typically 50–100 microns, compared to many millimeters for wire-based structures. These devices are now known under the common name of micropattern gaseous detectors (MPGDs).

Microstrip gas chamber (MSGC)

The first such structure to gain popularity was the microstrip gas chamber [10] (MSGC), of which the field pattern is shown in the third picture in figure 1.3. The principle of an MSGC resembles a wire chamber, with fine printed strips instead of thin wires, see figure 1.4. Due to the microelectronics techniques employed in manufacturing the spacing between anode strips was as narrow as 200 microns, compared to at least several millimeters for wire chambers. Most ions created in the avalanche process drift to the wider cathode strips, which are spaced only 60 microns away from the anodes. This short drift path for ions overcomes the space charge effect present in wire

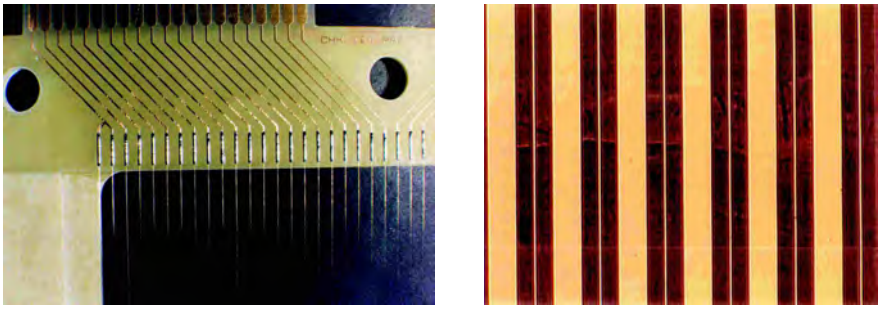

Figure 1.4 — Left: wires of a multiwire proportional chamber (MWPC) soldered to a frame. Right: microscope image of a microstrip gas chamber (MSGC)

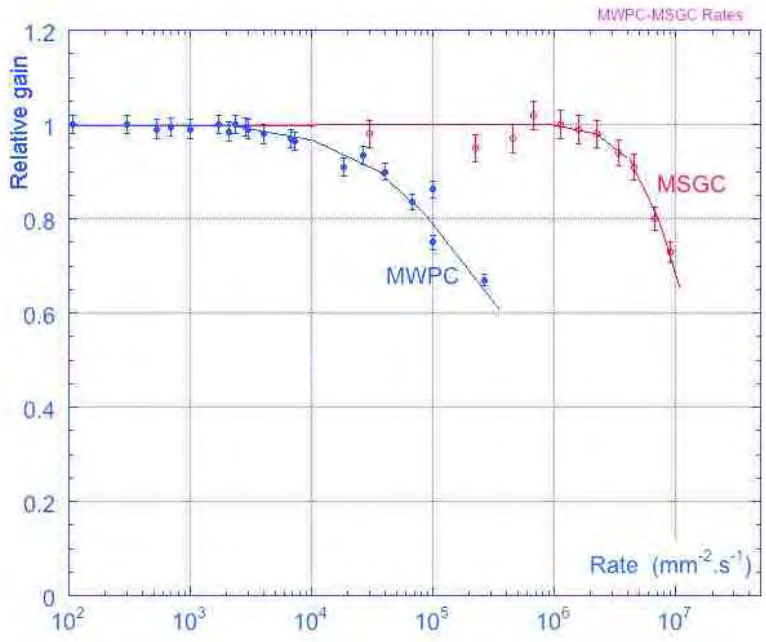

Figure 1.5 — Gain as a function of particle rate in otherwise constant conditions, for wire chambers in blue and MSGCs in red. [11]

chambers, where the slowly drifting ions may remain in the gas volume for milliseconds, and modify the electric field (thereby reducing the gain). Figure 1.5 shows how this space charge effect limits the rate capability of wire chambers, and how the fine granularity of MSGCs pushes this limit by two orders of magnitude.

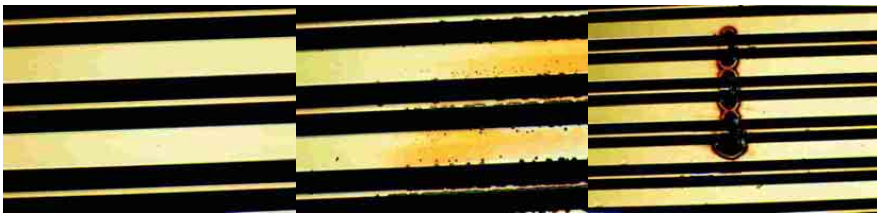

Figure 1.6 — Damage done to MSGCs by discharges. The left frame shows a new MSGC. In the middle frame one can see the impact of sparks on the electrodes (the little dark spots). In the right frame anode strips are cut by a strong discharge, leaving part of those anodes inactive. With its very thin metal layers MSGCs are particularly vulnerable for discharge damage.

The high rate capability of the MSGC made it an attractive technology for many applications. However, the development of the MSGC also showed some new limitations, most of which are common to all micropattern devices. One common issue is the charging of insulating surfaces which modifies the field shape locally, limiting the time stability. For MSGCs this could be solved by surface treatment of the glass substrate to decrease the surface resistivity.

Possibly most important is the issue of discharges, which eventually led high-energy physics experiments to abandon MSGC technology. MSGCs suffered severely from such discharges, induced by heavily ionizing particles or high particle rates, which could fatally damage the fragile anode strips, see figure 1.6. In 1997 the gas electron multiplier (GEM) was introduced [12] as a preamplification stage for the MSGC. This allowed the MSGC to work at a lower voltage, thereby lowering the probability of discharges as well as the energy involved in discharges when they occurred. The GEM principle was so successful that it soon became the basis for a detector in its own right.

Gas electron multiplier (GEM)

The gas electron multiplier is a copper clad polyimide foil with a regular pattern of densely spaced holes, see figure 1.7. Upon applying a voltage between the top and bottom electrodes, a dipole field is formed which focuses inside the holes where it is strong enough for gas amplification. As a GEM is only an amplification structure, it is independent of the readout structure, which can be optimized for the application (see a few examples in figure 1.8). Due to the separation from the readout structure, possible discharges do not directly impact the front-end electronics, thus making the detector more discharge tolerant. Also, it can be cascaded to achieve higher gain at lower GEM voltage, which decreases the discharge probability, see figure 1.9. The triple GEM has now become a standard which is used in many high rate applications [14, 15, 16].

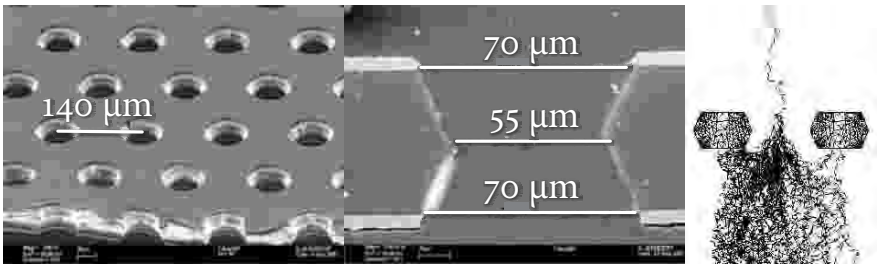

Figure 1.7 — Electron microscope images of a GEM foil: oblique perspective (left) and in cross-section (middle). On the right a simulated electron avalanche in a GEM hole. Also the diffusion of electrons is simulated, resulting in the irregular trajectories shown.

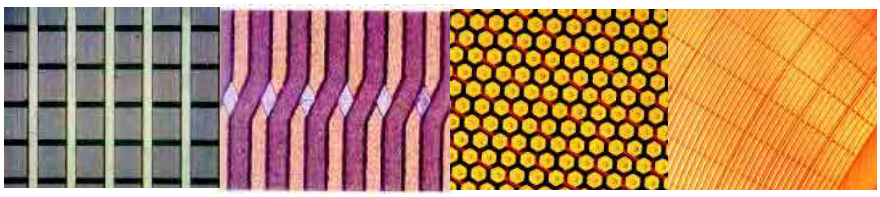

Figure 1.8 — Some examples of readout structures developed for GEM detectors.

Micromesh gas detector (Micromegas)

Another detector structure developed about the same time is the micromesh gas detector, or Micromegas [17]. This detector has a parallel plate geometry with the amplification gap between a metallic micromesh and the readout board. Parallel plate amplification existed before, but the Micromegas has a much narrower amplification gap of around 50–100 µm. The narrow amplification gap provides fast signals and a high rate capability. The micromesh is supported by regularly spaced pillars which maintain the accurate spacing. This is shown in figure 1.10.

1.3 Current trends in mpgds

The development of MPGDs took off in the 1990s mainly as a way to achieve a higher rate capability with gaseous detectors. Since then applications have driven developers to exploit the additional benefits of these structures, such as excellent time and position resolution, resistance to aging, and intrinsic ion and photon feedback suppression. Advances in available techniques for microelectronics and printed circuits opened ways to make new structures

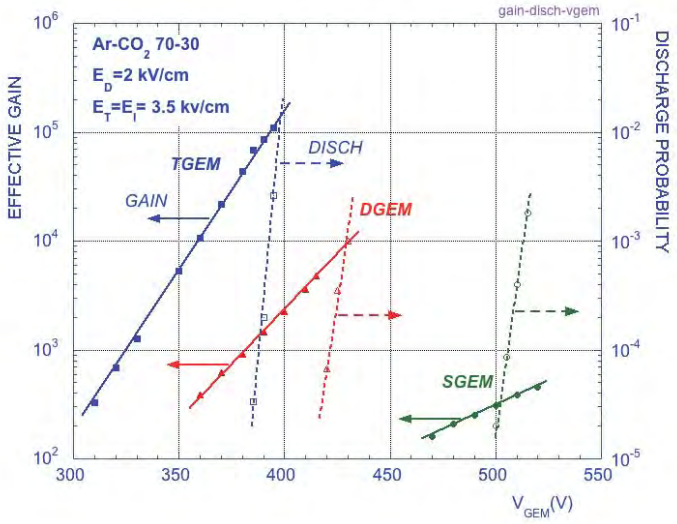

Figure 1.9 — Gain (solid lines, left scale) and discharge probability (dashed lines, right scale) as a function of GEM voltage, for single (SGEM), double (DGEM) and triple GEM (TGEM) detectors [13]. Discharge probability is measured by irradiation with α-particles, which deposit ~ 100 times more energy in the gas than MIPs (see section 1.1.1).

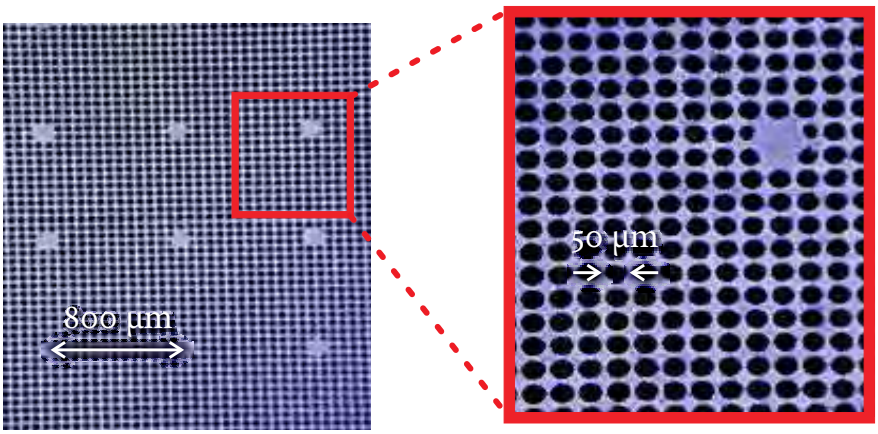

Figure 1.10 — Microscope images of a Micromegas detector, with indicated mesh and pillar spacings.

and optimize existing ones. This led to a wide range of detector structures for an even wider range of applications, with a performance superior to any traditional gas detector.

1.3.1 Techniques

The techniques that enabled the advent of micropattern gas detectors come from the industry of microelectronics and printed circuits. The microstrip gas chamber is made by employing photolithographic techniques used by microelectronics manufacturers. Instead of silicon wafers, thin glass plates are used as a substrate for printing the fine strip patterns. These glass plates are doped or sputter coated with so-called Pestov glass in order to reduce slightly the surface resistivity, which improves the time stability [18].

The very thin metal layers of MSGCs (few hundred nanometers) makes them vulnerable for discharges, which can easily do fatal damage (figure 1.6). Many of the later micropattern devices use thicker metals (few microns), and performance is normally unaffected by thousands of discharges. The techniques used to pattern these metals and the insulators separating them come from the manufacturing of printed circuit boards (PCBs). An advantage is the much lower cost, and the possibility to cover larger areas. These techniques include photolithography, metal etching and screen printing.

A rather special technique, thoroughly refined in the CERN PCB workshop, is the etching of polyimide. This is the basis of a number of micropattern gas detectors, including the GEM. Another method to pattern insulators, more standard in industry, is using photo-imageable polymers such as photoresist, coverlayers and solder masks.

1.3.2 Technologies

A few of the most prominent micropattern gas detector technologies have been mentioned in the introduction. Many more structures were developed and are currently used, which are often derived from MSGC, GEM or Micromegas. A few more examples are discussed here, but the selection is by no means exhaustive.

Polyimide structures

The refinement of the polyimide etching technique that is used to make GEMs, is also used for some detectors with a readout structure in the same plane as the amplification structure. These are the *WELL* [19] and the *groove detector* [20]. Unlike the GEM these structures are not "transparent", all the electrons from the avalanche are collected on the bottom electrode which is also the readout structure. The *microhole and strip plate* [21] combines the amplification mechanisms of GEM holes and microstrips (see figure 1.11,

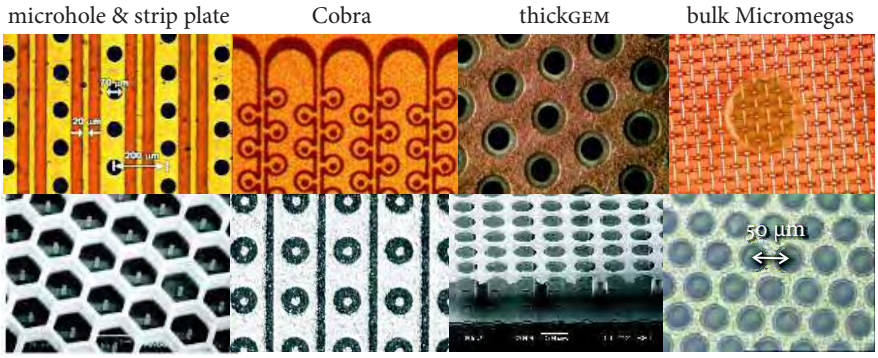

Figure 1.11 — Microscope images of various detector structures. See text for details on each frame.

first frame), and combines a high gas gain with an excellent ion feedback suppression. The Cobra structure [22], shown in the second frame of figure 1.11, was designed to enhance the ion feedback suppression further by an order of magnitude.

ThickGEM

Another GEM-derivative is the *thickGEM* [23], also shown in figure 1.11. This is a hole-type amplification structure, where the flexible polyimide substrate is replaced by a thicker glassfiber-reinforced-epoxy plate and the holes are mechanically drilled. The substrate is the standard base material for rigid PCBs and is therefore cheap, and readily available from any PCB manufacturer. Also the automatic drilling of the holes is a standard industry procedure. One has full control over the hole pitch and diameter, and the shape, size and thickness of the base material. These structures are convenient for applications where position and time resolution are not the most critical parameters, but which require a high gain and a certain ruggedness. ThickGEMs are for instance popular for photodetector applications, where the stiff substrate lends itself well to the vacuum deposition of a CsI photoconverter [24]. More recently, electrodes of thickGEMs have been covered with or replaced by resistive layers [25]. These detectors are reported to work stably in streamer mode, due to the enhanced quenching by the resistive layers.

Bulk Micromegas

Micromegas detectors underwent a technical improvement with the introduction of a new fabrication method [26]. Here a woven metal micromesh is laminated to the readout board between layers of photoimageable soldermask. These soldermask layers can subsequently be patterned by UV-exposure to create the supporting pillar structure (see the fourth frame of figure 1.11). The materials involved are quite inexpensive, and the processes are industry

standard, which makes it suitable for large scale production. Also, the homogeneity of the grid spacing is better than of the original Micromegas detectors, and the detector is very robust.

Micropin, microdot

The *micropin array* [27] was introduced for x-ray imaging (see figure 1.11, first frame of the second row). The spherical geometry of the electric field close to the end of each pin (proportional to $1/r^2$ compared to $1/r$ of a wire chamber) gives rise to very short amplification region, allowing a rate-stable high gain. A similar philosophy led to the development of the *microdot chamber* [28](also shown in figure 1.11, for which microelectronics techniques were employed to reach feature sizes of only a few microns.

Pixel readout

The coming of age of *post-wafer processing* techniques marked the introduction of MPGDs with pixel readout. These detectors use the bump-bonding pads of a pixel chip as a readout structure. The position and time resolution of these devices is unmatched by any other gas detector. Due to their high sensitivity they can distinguish each primary electron. This enables them to resolve delta-rays from a track or to reconstruct the direction of emission of a photoelectron from an x-ray conversion (related to the x-ray polarization). One group uses a Micromegas-type of gas amplification: *InGrid* [29]. The grid electrode and the insulating pillar structure supporting it are made directly on the chip by post-wafer processing techniques, allowing the grid holes to be aligned with the readout pads (see figure 1.11). Another group uses an ASIC with a hexagonal readout pad structure, and a GEM-based amplification structure [5]. Here the GEM has a reduced pitch of 50μm and thickness of 25μm (compared to 140μm and 50μm respectively for standard GEMs) to match the granularity of the readout (see the last frame of figure 1.11).

1.3.3 Applications

Micropattern gas detectors have already been applied in many instruments and experiments, both by science and industry. Possible fields of application are high-energy and nuclear physics, synchrotron and thermal neutron research, medical imaging and homeland security. Most structures were primarily developed for high rate tracking of charged particles in nuclear and high-energy physics experiments. For instance Micromegas [30] and GEMs [14] are used in the COMPASS experiment, and GEMs in LHCb [16] and TOTEM [15] experiments. Also for the LHC machine upgrade program to increase its luminosity by roughly a factor of ten, most of the experiments foresee replacement of wire chambers, drift tubes and resistive plate chambers by MPGDs. However many MPGDs have shown to be suitable for other applications as well. A few examples are given here.

Tpc

Both GEMs and Micromegas can be used for the readout of a time projection chamber [31] (TPC). Compared to wire chambers, these MPGDs have the benefit that the planar structure suppresses the $\mathbf{E} \times \mathbf{B}$ effects which limit the spatial resolution of wire chambers in a TPC configuration. Also, both Micromegas and GEMs have a natural ion feedback suppression, which may make a gating structure unnecessary. If a high granularity readout structure like a pixel chip is used, the excellent spatial and energy resolution can resolve primary clusters, improving the measurement of energy loss.

Photodetection

As mentioned before, GEM-like structures can be coated with a photoconverter (typically CsI) to serve as a photon counter. In this way, large areas can be covered with hardly any dead zones, and the technique is inexpensive. This makes it attractive for ring imaging Cherenkov detectors, where the photodetector planes often span several square meters. Also here the ion feedback suppression is an added benefit, as it increases the lifetime of the photoconverter. In addition, the detector can be made "hadron-blind" by reversing the drift field, and even "windowless" if the Cherenkov radiator gas (in that case typically CF_4) is also used as amplification gas [32].

X-ray detection

X-ray counting and imaging detectors can be based on MPGDs [33], as x-rays convert in some noble gases leaving typically few hundred primary electrons for detection. For these purposes efficient x-ray conversion gases are frequently used, such as xenon or krypton. Argon is about an order of magnitude less efficient, but so much cheaper that it can still be attractive for high rate applications.

Neutron detection

Microstrip gas chambers and GEM detectors are also used as neutron detectors [34]. A boron layer (in the form of $^{10}B_2O_3$) can be vapor-deposited onto GEM foils, which acts as a neutron converter. For the best efficiencies gaseous converters are used at high pressure: ^{3}He or $^{10}BF_3$. Conversion reactions and cross-sections are given in table 1.1.

1.3.4 Performance

Depending on the application, the performance of MPGDs has different figures of merit. The first MPGDs were designed to obtain a high rate capability. Several MHz/mm² of charged particles are easily reached with, for instance, a triple GEM detector, without a measurable loss of gain and with negligible discharge probability.

Resolutions

Time, position and energy resolution are crucial figures for most applications. GEM-based detectors normally have a position resolution of about 50 µm, Micromegas can go down to ~ 12μm if equipped with a high density readout board. Time resolutions are of the order of few nanoseconds. X-ray

energy resolution is often measured using a ^{55}Fe source, obtaining a FWHM between 15% and 22%. MPGDs with pixel chip readout report position resolutions below 10 μm and a time resolution of 1 ns. From the ^{55}Fe spectrum they can resolve the K_α and K_β energies, and reach a resolution of 12%.

Ion feedback

The reduction of ion backflow into the drift region is a general property of MPGDs. It is usually expressed as a fraction of the effective gain, and this value depends quite strongly on the way the fields are configured in the chamber. Microhole and strip plates feature a particularly effective ion feedback suppression of the order 10^{-4} in optimized conditions. Combined with a Cobra structure, 10^{-5} has even been realized [22].

Aging

Aging modes of gas detectors are largely understood in the case of wire chambers [35]. There the plasmas that are formed during avalanches in the strong field near the wire deposit layers of silica or polymers which reduce the gain and give rise to micro discharges. Most micropattern devices do not generate such a strong field at the surface of the conductors, and consequently little signs of aging have been observed. Specific aging studies of MPGDs have rarely been done yet, and time will prove if they are as resistant to aging as it seems.

1.4 An r&d collaboration for mpgds

RD51 is a large R&D collaboration, which unites many institutes in an effort to advance technological development of micropattern gas detectors [36]. At the time of writing there are ~ 430 participating authors from 73 institutes in 25 countries worldwide. The efforts of the collaboration do not focus on one or a few particular applications for MPGDs, but is rather *technology oriented*. It is a platform for sharing of information, results and experiences, and for steering R&D efforts. It tries to optimize the cost of R&D projects by sharing resources, creating common projects and providing common infrastructure.

RD51 has two co-spokespersons. Concerning all scientific matters the collaboration is governed by a *collaboration board* (CB), which is also responsible for coordinating the financial planning and other resource issues, in particular for managing the common fund. Representatives from all collaborating institutes are seated in the CB, and have voting rights. A *management board* (MB) supervises the progress of the work program along the lines defined by the CB and prepares decisions for and makes recommendations to the CB.

The activity is divided in seven working groups (WGs), covering all relevant topics of MPGD-related R&D. A number of tasks is assigned to each working group. Table 1.2 lists all the WGs and indicates their objectives and tasks.

Table 1.2 — Organization of RD51 in working groups and tasks.

	WG1 MPGD technology & new structures	WG2 Characterization & physics issues	WG3 Applications	WG4 Software & simulation	WG5 Electronics	WG6 Production	WG7 Common test facilities
Objectives	Design optimization. Development of new geometries and techniques	Common test standards. Characterization of physical phenomena in MPGDs	Evaluation and optimization for specific applications	Development of common software and documentation for MPGDs	Readout electronics optimization and intergration with MPGDs	Development of cost-effective technologies and industrialization	Sharing of common infrastructure for detector characterization
Tasks	Large area MPGDs — Design optimization New geometries Fabrication — Development of rad-hard detectors — Development of portable detectors	Common test standards — Discharge protection — Aging and radiation hardness — Charding-up and rate capability — Avalanche statistics	Tracking and triggering — Photodetection — Calorimetry — Cryogenic det. — X-ray & neutron imaging — Astroparticle physics appl. — Medical appl. — Plasma diagn. Homeland sec.	Algorithms — Simulation improvements — Common platforms (ROOT, Geant4) — Electronics modeling	FE electronics requirements definition — General purpose pixel chip — Large area systems with pixel readout — Portable multi-channel system — Discharge protection strategies	Common production facility — Industrialization — Collaboration with industrial partners	Testbeam facility — Irradiation facility

Wg1 Wg1 is concerned with the technology of mpgds and the design of new structures. Examples are efforts to make Micromegas, gem and thickgem technologies suitable for large areas [37]. Also interesting is the development of cylindrical gem [38] and Micromegas [39] detectors for inner barrel tracking. A recent development is the introduction of spherical gems [67] for parallax-free x-ray diffraction measurements.

Wg2 The second working group deals with physics issues of mpgds, such as discharges, charging of dielectric surfaces and aging. Also, common test standards are proposed to enable different groups to compare their results. Regular meetings have become a forum for exchanging results and for discussion about what are actually the most fundamental properties of micropattern gas detectors.

Wg3 Wg3 concentrates on the applications of mpgds, and on how to optimize detectors for particularly demanding applications. Examples have been listed above and new applications still appear, sometimes from surprising fields: one project aims to construct very large area gem chambers to detect nuclear fission materials or waste in cargo containers by tomography of cosmic ray muons [40].

Wg4 Wg4 develops simulation software and makes progress in the field of simulation. Simulation is essential to understand the behavior of detectors. A mature range of software tools is available for simulating primary ionization (Heed[1]), electron transport properties in gas mixtures in electric and magnetic fields (Magboltz[2]), and gas avalanches and induction of signals on readout electrodes (Garfield[3]). Garfield has interfaces to Heed and Magboltz and only needs to be supplied with a field map and detector configuration. A field map can be generated by commercial finite-element method (fem) programs such as Ansys, Maxwell, Tosca, QuickField and Femlab. Within the collaboration, an open-source field solver is being developed and recently released called nebem [41]. It is based on the boundary element method (bem), and is in most respects superior to fem solvers for gas detector simulations.

Wg5 Front-end electronics and data acquisition systems are discussed in wg5. Electronics for detectors are highly specialized and therefore almost entirely based on application specific integrated circuits (asics). A front-end asic often has to be radiation tolerant, must accept external triggers and have long analog pipelines for the trigger latency, and must support high output data rates. Availability, flexibility and scalability of chips and daq systems are discussed in regular meetings. Mpgds have typically one more requirement

[1] Author: Igor Smirnov (http://consult.cern.ch/writeup/heed/)

[2] Author: Stephen Biagi (http://consult.cern.ch/writeup/magboltz/)

[3] Author: Rob Veenhof (http://garfield.web.cern.ch/garfield/)

for the front-end chip: it must survive discharges, and the dead time following a discharge must be kept to a miminum. Various solutions are in development in this working group.

WG6 WG6 deals with the production of MPGDs. Almost all MPGDs were first made in the CERN PCB workshop of Rui de Oliveira, and it remains an almost exclusive manufacturing site for most technologies. Hence, efforts in WG6 are aimed at plans for upgrading this workshop on the one hand, and industrial partnership and export of the technology and know-how on the other. Also, scenarios are developed for industrial scale production of some MPGDs (especially GEMs and Micromegas), in case a large experiment decides to implement them in their system.

WG7 Finally, WG7 coordinates the effort to set up a shared test infrastructure in the form of test beam and irradiation facilities. The test beam facility will be equipped with supply and exhaust of gases, including flammable mixtures. Also a large 1.4 Tesla magnet will be provided. The irradiation facility provides a strong gamma source (a 10 TBq ^{137}Cs source is foreseen) combined with a 100 GeV muon test beam (10^4 muons per spill) and is called GIF++ [42].

Chapter Two

GEMS

Now that the principles of gas detectors, and more specifically the benefits of micropattern gas detectors have been introduced, this chapter goes into details about the gas electron multiplier (GEM). After a few examples of applications in high-energy physics, the process of design, manufacturing, assembly and testing of GEM detectors is described.

2.1 Applications

GEMs have already been applied in many detectors, both in high-energy physics and in other fields. As an example, some of the most visible applications in high-energy physics are discussed below. Table 2.1 gives a summary of the required parameters for these applications.

2.1.1 HERA-B

The first application of GEMs was in the HERA-B experiment at DESY, Hamburg [43]. There it served as a preamplifier for an MSGC, to cope with rates of up to 10^6 particles per cm^2 per second. Ten stations of several detectors each were distributed along the beam pipe, three of them inside the magnet (B = 0.85 T). They were used both for precision tracking (better than 100 µm) and momentum measurements, and for triggering with 99% efficiency for a pair of detectors. The glass of the MSGCs was coated by chemical vapor deposition with an amorphous carbon composite, to reduce the surface resistivity to 10^{14}–$10^{15}\,\Omega/\square$ and thereby improve the time stability.

Table 2.1 — Some applications of GEMs in high-energy physics experiments, and the required parameters of the detectors.

Experiment	Purpose	Config.	Size (cm^2)	Space res.	Time res.	Rate cap.
HERA-B	track/trig.	GEM+MSGC	30 × 30	100 µm		1MHz/cm^2
COMPASS	tracking	triple GEM	31 × 31	46 µm	15.0 ns	150kHz/cm^2
LHCb	triggering	triple GEM	24 × 20		4.5 ns	500kHz/cm^2
TOTEM	track/trig.	triple GEM	30 × 16	58 µm	10.0 ns	1MHz/cm^2

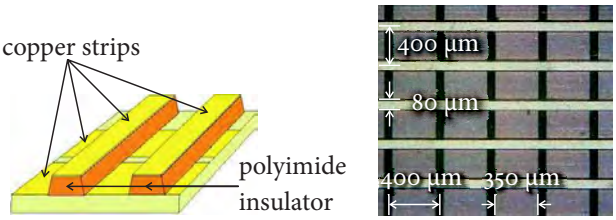

Figure 2.1 — The XY-readout structure developed for the COMPASS triple GEM detectors. On the left, a reconstruction of the buildup in layers. Dimensions are indicated on the photograph to the right.

2.1.2 *COMPASS*

COMPASS is a fixed-target experiment at CERN. It includes 10 stations of two triple-GEM chambers each [14]. A lot of pioneering work was done for this first application of triple GEM detectors. Many of the solutions found for the technical challenges have become standard practice in later applications. Therefore these detectors will be described in greater detail than the other examples.

Readout board

The readout board has fine-pitch X and Y strips, for an accurate 2D position readout. To measure both cartesian coordinates of the same event, the charge coming from the triple GEM structure must be collected by both horizontal and vertical strips in roughly equal shares. In addition, the charge is shared by several strips of the same coordinate to improve the position resolution of reconstructed clusters. To meet these conditions, the strip pitch of both coordinates must be substantially smaller than the diffusion width of the charge cloud (defined in section 1.1.2). Figure 2.1 shows how this is achieved with strips in two directions located in separate planes. With this readout technique a spatial resolution of 46 µm is obtained for both X- and Y-coordinates.

Sharing of charge between X and Y strips is done by optimizing the relative width of both sets of strips. The charge sharing ratio can be accurately controlled, so that it assists in disentangling events with multiple hits, in case one hit leaves more ionization than the other. The pattern in the insulating layer that separates the layers of strips is made by the same polyimide etching technique that GEMs are also based on.

HV distribution

In this first application of triple GEM detectors substantial effort was spent on supplying and distributing the 7 high voltage potentials to the respective electrodes. A key issue was the prevention of discharges and especially their propagation (from GEM to GEM, or from GEM to readout). The HV distribution

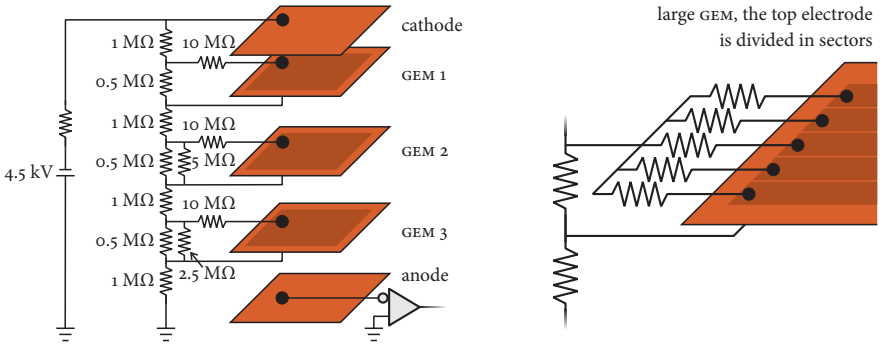

Figure 2.2 — Resistive divider for distribution of high voltages to all the electrodes of a triple GEM detector, all values are indicative. In case the electrodes are large (right), they are segmented and each segment is powered through its own safety resistor.

scheme turns out to be instrumental to reach these goals [13]. Figure 2.2 shows a typical HV distribution network frequently used for triple GEMs. It is a resistive divider, where the top electrodes of GEMs are supplied through high-value safety resistors. These safety resistors limit the current that recharges the capacitance that is being discharged by a spark, thereby quenching the gas discharge. By applying those resistors to the top electrodes only, their potential drops in the event of a discharge, leaving the voltage of bottom electrodes stable. The electric field strength above the GEM (towards the drift cathode) will thus increase, but not below the GEM (towards the readout). This makes propagation of a discharge very unlikely, as gas discharges normally propagate from cathodes to anodes. Direct impact of a spark onto the readout electrode (and the sensitive electronics connected) is unlikely with this distribution scheme. The ratio of gain to discharge probability can be further optimized by applying a slightly different voltages to the three GEMs, with the first about 10 % higher and the third about 10 % lower than the second one. This is indicated in figure 2.2 as parallel resistors in the divider.

Sectors

Due to the short distance between top and bottom electrodes (50 µm) and the presence of a dielectric (κ = 3.3), the capacitance of a GEM can be rather high compared to other micropattern structures. To limit the energy transferred in a discharge, the top electrode is divided in sectors with each sector up to 100 cm^2. This corresponds to a capacitance of about 4.7 nF. Each sector is connected to the divider through a separate safety resistor. This way, only the capacitance of one sector is involved in a discharge, all other sectors are unaffected. The recovery time of a sector depends only on the value of the safety resistor and the area of the sector: $RC = 10^7 \cdot 4.7 \cdot 10^{-9} = 0.047$ s

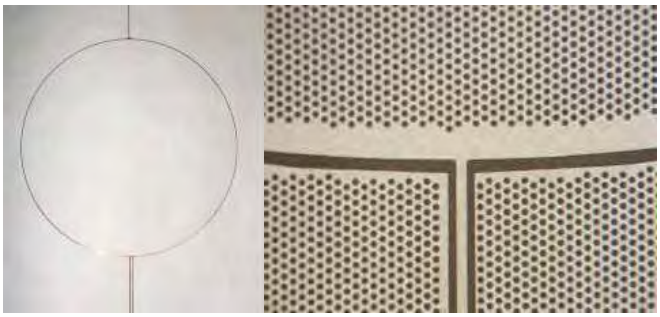

Figure 2.3 — Beam killer region in the middle of the COMPASS GEMs. In case the particle rate is too high the gain in this sector can be reduced to zero by shorting it with the bottom electrode of the GEM.

or 47 ms for 10 MΩ and 100 cm². Sectors are separated from each other by a clearance of 100 µm, this is found to be sufficient to avoid sparks from propagating from one sector to another.

A special feature of the COMPASS GEMs is the so-called *beam killer*. This is a sector on the top electrode of each GEM, formed such that it covers the area where the beam goes through the detectors, see figure 2.3. In this region the rate can be so high (depending on beam particle type and the target) that the occupancy of the strips covering it becomes intolerably high. The beam killer sector can be "switched off" by shorting it with the bottom electrode.

The way the triple GEM detectors for COMPASS were assembled is still the most conventional method, it is illustrated in figure 2.4. GEMs are stretched and glued to spacer frames, which are wide along the border of the chamber and which have very slim elements (~ 300 µm) in the active area to keep accurate and uniform spacing between layers. To the right of figure 2.4 is one such spacer frame used for the COMPASS detectors. The thin spacer elements inside the active area may be necessary or not, depending on stretching tension and size of the detector. In this case it was deemed necessary, even though close to these elements minor inefficiencies were reported. Light aramid honeycomb panels back the front and rear faces of the detector for protection and mechanical rigidity.

2.1.3 LHCb

LHCb is an LHC experiment aimed at heavy flavor physics. Twelve pairs of triple GEM detectors (see figure 2.5) are used as muon trigger stations in the forward region where the rates are very high (up to 10 kHz/cm²) [16]. As

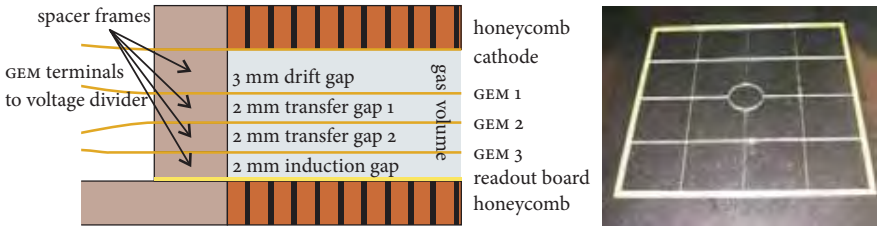

Figure 2.4 — Left: composition of COMPASS triple GEM chambers. Most triple GEM detectors built later used the same or similar methods. Right: a COMPASS GEM spacer.

spatial resolution is not a concern, a readout structure of large pads (1×2.5 cm^2) is used. Much effort was spent on optimizing the time resolution at high efficiency. This resulted in a resolution of 3.5 ns and an efficiency of ~ 97 % per station, or 4.5 ns and ~ 90 % per detector, working at a gain of only 4000.

These extraordinary figures are reached by a combination of choices for design and gas mixture. A ternary gas mixture of Ar/CO_2/CF_4 (45%/15%/40%) is used because of its high electron drift velocity (~ 10 cm/µs) and high primary cluster yield (~ 7 mm^{-1}). The induction gap is reduced to only 1 mm to have a steeper signal rise time, hence reducing *time walk*. The first transfer gap is also reduced to 1 mm to limit the amount of ionization charge deposited in that gap; this charge could lead to a premature signal.

2.1.4 TOTEM

The TOTEM experiment is another LHC experiment, integrated in the very forward regions of the CMS experiment. Because of its specific physics programme and its forward coverage, it cannot rely on the CMS trigger system and it needs to generate its own triggers. Each of its three subdetectors (from up- to downstream: cathode strip cambers, triple GEMs and roman pots) are therefore designed as self-triggering units.

The 40 GEM detectors have a semi-circular shape which allows them to embrace the beam pipe from both sides (see figure 2.5). To combine tracking and triggering functionalities the readout board consists of 512 concentric strips (tracking) on top of 1560 pads (triggering). Between pads and strips charge is shared by the same technique presented above for the COMPASS GEMs (figure 2.1). A time resolution of below 10 ns is reached with a "standard" gas mixture of Ar/CO_2 (70%/30%), which is also used by the HERA-B and COMPASS GEM detectors.

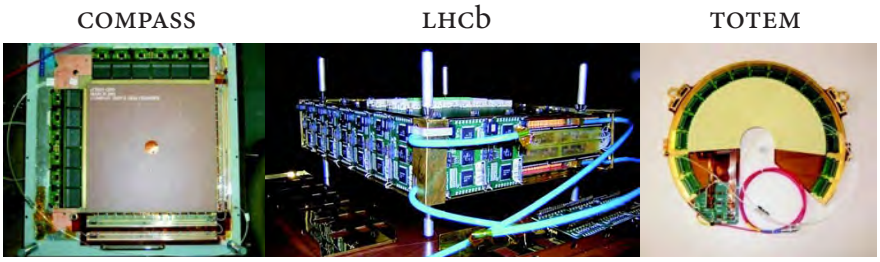

Figure 2.5 — Examples of final detector assemblies of applications discussed in the text.

2.2 Design & assembly

Design of a GEM detector is not straightforward. It involves many components and is built up in several layers, all of which must align well with the others. Also assembly of GEM-based detectors poses certain challenges: alignment, gas tightness and most of all the stretching of GEM foils. These aspects of GEM technology are discussed in the following sections.

2.2.1 *Design*

Design of a GEM detector typically comprises the GEMs themselves, spacer frames, honeycomb panels, a readout board and a high voltage distributor. One can use *computer aided design* (CAD) software for defining accurately the shape and dimensions of each layer, and add alignment features (holes for dowel pins, reticles) on all layers to facilitate assembly later. The output formats of CAD software, most conventionally `.dwg` or `.dxf` files, can be interpreted by *computer aided manufacturing* (CAM) software, which in turn can output fabrication scripts for manufacturing.

GEMs

What needs to be specified in a design for a GEM foil is the areas that must be filled with holes, and the top and bottom electrodes. As noted in previous chapter, the fabrication is done with methods and procedures from the printed circuit board (PCB) industry. Therefore, PCB design software can be used with the benefit of having a fabrication output format native to PCB manufacturing equipment: Gerber files.

Proper segmentation of the top electrode must be included in the design (if > 100 cm^2), with 100 µm spacing between sectors. No GEM holes should be put in the gap between sectors, or too close to the edge (typically another 100 µm margin). There should also be some margin (~ 2 mm) between the active area (where there are holes) and the frame, to allow some tolerance

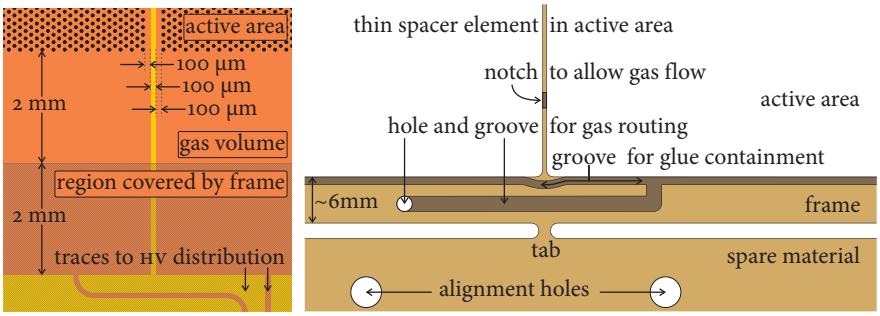

Figure 2.6 — Schematic explanation of design features introduced in the text. Left: the most relevant parameters in the design of a GEM, with segmented electrodes extending into the region covered by the frame. Right: a spacer frame with features to contain the flow of excess glue, to route the gas, and to align the frame with respect to others. Note the different length scale left and right.

for assembly and to prevent excess glue from entering holes. It is considered good design practice to let the electrodes extend far enough outside the active area that the outer edge (~ 2 mm) is covered by the frames after assembly. This way the amount of exposed dielectric is minimized, and an imperfect shape of the edges will not provoke discharges. All this is indicated in figure 2.6 (left).

The design of the electrodes must include terminals to eventually connect the GEM to the high voltage circuitry. Hence, even if the high voltage divider is not yet designed, its placement and features are constrained by the design of the GEM. Care must be taken to ensure compatibility of high voltage terminals with the foreseen gas distribution scheme and signal lines.

Frames

Frames are usually made from plate material of well-known and uniform thickness[1], from which material is removed by a *numerical control* (NC) milling bench. The spacer frames between electrodes consist of a strong perimeter for mechanical strength, and thin features in the active area (if necessary) to minimize adverse effects on the efficiency. Spare material outside the frame can be kept in one piece with the frame, attached by so-called *tabs*, short interruptions in the routing of the board cutout, see figure 2.6 and also 2.7. This spare material facilitates handling along the assembly process, it lends stiffness to the frame and one can design alignment holes on it (shown to the right of figure 2.7). Tabs can be applied at regular intervals along the

[1]Very often used are Permaglas plates from Permali, distributed by Resarm Engineering plastics. These are fiberglass-reinforced epoxy panels made of thin, non-woven fibers with good mechanical properties, radiation hardness, and low outgassing.

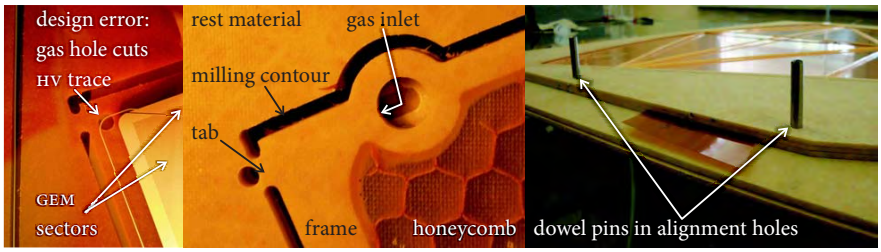

Figure 2.7 — A few examples of design elements discussed in the text. Left panel: by a design mistake, a trace of the high voltage routing runs through a hole in the frame meant to transport gas. The middle panel shows the correction of this mistake: the gas is entered through the honeycomb panel, away from the HV trace, then channeled through a groove in the spacer frame. The right panel shows the use of alignment holes in the spare material around the frames, connected through *tabs* (shown in left and center panels).

perimeter, and especially at places where more stress can be expected (for instance opposite to a thin spacer element reaching into the active area, as in figure 2.6).

The honeycomb panels that are conventionally applied to top and bottom of each chamber need frames too, to enclose the honeycomb regions with more rigid support. Gas distribution features are often included in the design of frames. Grooves in frames and aligned holes through several layers can inject and extract gas wherever it is considered optimal. Also the thin spacer elements in the active area should have notches to facilitate gas flow and route it in a sensible way, avoiding *pockets* where flow will be negligible. All these features are indicated to the right of figure 2.6. A very useful additional feature for a spacer frame is a *glue containment groove* along the inside of the frame. It prevents excess glue from creeping towards the GEM holes (glue is not a strong dielectric); see in figure 2.6 how it is routed to avoid making the thin spacer elements more fragile than they already are. If aligned holes are used to transport gas through different layers, care must be taken to avoid cutting high voltage or signal traces (such an error is shown to the left of figure 2.7).

Readout boards

The design of the readout board is closely linked to the application of the detector. It is essentially a PCB and can be designed with any of the software packages available. The active area should coincide with the area covered by GEM holes, and it should include grounding and screening features.

Signal integrity is not granted, and it is recommended to keep signal traces as short as reasonably possible. A way to connect the signal traces to front-end electronics must be foreseen, especially in case integrated multichannel elec-

tronics is used. In that case high pitch board-to-board connectors[2] are often used to avoid wire-bonding ASICs (application specific integrated circuits) directly to the readout board. The ASICs are then bonded to small outline, modular *hybrid PCBs* which can be plugged to the detector, and replaced whenever necessary.

2.2.2 *Assembly*

After all components are designed and manufactured, they must be assembled to make a complete detector. This means stretching GEMs and gluing them to spacer frames, building stiff panels from frames and honeycombs, and stacking up all layers (including drift electrode and readout board) to complete the chamber. Before and after each step in which GEMs are manipulated, high voltage tests should be done to verify that there are no sparks and leakage current stays at few-nA level. The following will go through these steps in a bit more detail.

Framing GEMs

The GEM foils need to be glued to their respective frames. To avoid any distortions of the electric field above and below the GEM, the foil should be stretched before the frame is glued to it. There are basically two methods to do this: *thermal stretching* and mechanical stretching.

With thermal stretching, a foil is firmly attached (usually by clamping) to a rigid frame made of a high coefficient of thermal expansion (CTE) material, and then frame and foil are heated. Once a thermal equilibrium has established, the spacer frame (of low CTE) is glued to the stretched GEM, and both frames and the GEM are kept warm until the glue has hardened. In the left panel in figure 2.8 a spacer frame has just been glued to a stretched GEM, and is about to be put back in an oven to finish curing the glue. Upon cooling down the active area of the GEM foil can only shrink according to the CTE of the spacer frame, so the strain of the GEM can be expressed as:

$$\varepsilon_{\text{GEM}} = \text{CTE}_{\text{high}} \cdot \Delta T - \text{CTE}_{\text{low}} \cdot \Delta T = \left(\text{CTE}_{\text{high}} - \text{CTE}_{\text{low}}\right) \Delta T. \qquad (2.1)$$

This depends on the difference of expansion coefficients and is proportional to the temperature excursion.

For making the high CTE frame normally Plexiglas (PMMA) is used with a CTE of 70 ppm/K. Spacer frames are usually made of fiberglass-reinforced epoxy plates with CTE close to 15 ppm/K. Hence, with a typical working temperature of 45° C (ΔT = 25 K), the strain of the framed GEM is 0.14%. The

[2] For gas detectors, especially GEM-based, the Panasonic P5KS connectors have become a de facto standard. Part numbers for male: AXK6SA3677YG, and female: AXK5SA3277YG.

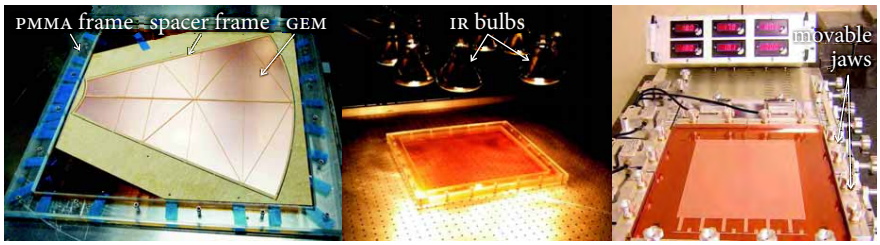

Figure 2.8 — Stretching and framing GEMs. Left and middle: thermal stretching using a PMMA frame, in the middle panel it is heated by infrared lamps, in the left panel it goes into a normal oven. Right: an LHCb GEM (discussed in previous section) mounted in a mechanical stretching jig. The displays all read 18 kg.

stress of the framed GEM equals the strain times the *tensile modulus* of the material. Unfortunately this parameter is not accurately known for GEMs. The polyimide[3] has a specified modulus of 4.1 GPa; the copper cladding will increase that value somewhat, and the hole pattern (~ 20% of the volume) will effectively decrease it again. If we accept the value of 4.1 GPa as indicative, we obtain a stress of 5.6 MPa.

An alternative to heating in a clean oven is shown in the middle frame in figure 2.8. This is a setup consisting of infrared (IR) light bulbs, temperature sensors and a control unit that uses the feedback of the sensors to limit the supply of power to the bulbs. The results from this system are similar to those from normal ovens, and this solution is cost effective if compared to the cost of a cleanroom grade oven.

Mechanical stretching is done using a jig designed for this purpose, and dimensioned to match the GEMs to be stretched (shown in the right panel in figure 2.8). The GEM foil is mounted in a number of jaws surrounding the region where the frame will be glued. Of each pair of opposing jaws, one is stationary and the other is moved outward to stretch the GEM. The force can be read out by gauges, so that a uniform and sufficient stress can be applied to the foil. The jaws in the figure are 18 cm wide, and the polyimide is 50 µm thick, so the stress in the foil is 20 MPa. With such a high stress the use of spacer elements in the active area can normally be avoided, this is also the case for the LHCb detectors.

Keeping spare material attached through tabs, as indicated in the section on design, is essential for helping the frames cope with the tension of stretching. Especially frames with complex shapes, like the ones for TOTEM mentioned above, have buckled under the stress of the foil before this tabbed

[3] Apical NP from Kaneka Texas Corporation.

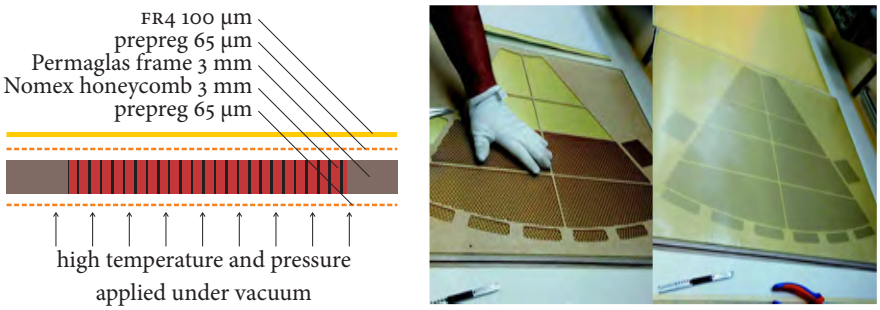

Figure 2.9 — Left: schematic buildup of the layers of a honeycomb panel. Right: two pictures of the preparation of a stack to be pressed in a vacuum oven.

routing became standard practice.

Honeycombs

Honeycomb material is available from many vendors, in various materials. For GEM detectors aramid fiber honeycombs have always been used as these have a favorable stiffness-to-weight ratio and are electrically insulating. Figure 2.9 (left) indicates how honeycomb panels are constructed. A stack of layers is prepared, with prepregs (woven fiberglass mats impregnated with uncured epoxy) acting as a double-sided adhesive, see the right of the figure, and then cured under pressure in a vacuum oven. The layers are not built up symmetrically because on one side the honeycomb must be covered by a permeable layer, to be compatible with the vacuum in the oven. The impermeable side, where a fiberglass sheet (marked FR4 in the figure) is added, will have a good flatness as this sheet is rather stiff. This is the side that will be turned toward the gas volume, to which the readout structure or the drift electrode is glued.

It would often be attractive to add a metal layer to the outside of a honeycomb panel for screening purposes. As long as the honeycomb cells need to be evacuated and vented through the surface of the prepreg this metal layer can only be added after finishing the honeycomb panel. There are however honeycomb materials available in which the cell walls are perforated. This could make it easier to add metal layers or reinforcements in the same process when the panel is made.

Final assembly

After all GEMs are stretched and framed, honeycomb panels are made, and the readout board and drift electrode are glued to their respective panels, the chamber can finally be assembled. Using alignment holes designed in the material around the frames, one can add layer after layer of glue-covered frames (see figure 2.10, left). Then pressure can be applied to the stack by putting weights on top, as long as the glue is curing. When the glue is dry,

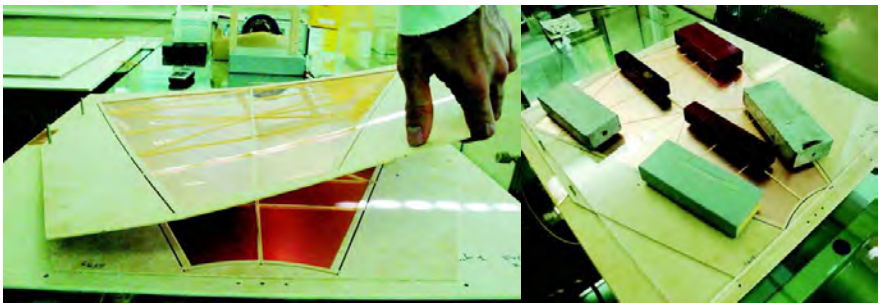

Figure 2.10 — Left: building up the stack of layers, using dowel pins in alignment holes on the extreme left. Right: when the stack is complete, pressure is applied by weights, while the glue is curing.

the tabs can be broken by sawing or drilling, and the spare material sheds off. The chamber is ready for leak testing.

Leak testing can be done with all conventional methods (for instance using a so-called sniffer), with the precaution that a chamber made in the way described above cannot stand a high over- or under-pressure with respect to ambiance. Gas leaks are often closed with a conformal coating meant for electronic circuits. The liquid coating will be wicked into narrow cavities and gas leaks by capillarity. As these coatings are meant for electronics, their dielectric properties are reliable. Depending on what type of readout structure is used there may be concerns about its tightness, especially if it has *vias* (metallized holes), in which case tightness may depend on the quality of gluing the readout board to its honeycomb panel.

Materials

Aging of gas detectors has always been closely linked to contaminations of the gas mixture [44]. These contaminations are either caused by outgassing of materials from which the chamber is constructed, or from decomposition of components of the gas mixture (or again construction materials of the chamber) under the influence of radiation. Radiation hardness and outgassing properties of materials are rarely specified in their datasheets. For this reason, groups developing gas detectors have usually stuck to materials of proven merit. Some outgassing studies were done at CERN for development of LHC detectors, materials can be picked from their list of tested materials[4].

[4] `http://detector-gas-systems.web.cern.ch/detector-gas-systems/Equipment/outgassing.htm`

2.3 Testing

Doing lab tests with GEM chambers one can assess their performance in terms of gain, resolution, rate capability or whatever property is relevant for the application. Radioactive sources can be used, or an x-ray tube, and finally a beam test can be done. Each of these tests has its merits, and all will be discussed in the following.

X-rays

Even though most GEM detectors are developed to detect high energy charged particles, measurements of properties of the detector are often better done with x-rays. There are several reasons for this. X-rays of a few keV (*soft x-rays*) deposit more charge in the drift gap (few 100 e^-) than *minimum ionizing particles* (MIPs, few 10 e^-), and can therefore be detected more easily with a non-optimized detector at a modest gain. The amount of charge deposited in the drift gap by MIPs is Landau distributed, and moreover depends on inclination angle. X-rays lose all their energy in a conversion, and the amount of charge is Gaussian distributed with a variation of about $\sigma_Q/Q \approx 5\%$, depending on gas mixture. This makes it possible to measure the energy resolution, as a measure of how well-controlled, uniform and stable the gas gain of the detector is. With an x-ray tube one can work at such high rates that the DC anode current can be measured (with a nA-meter). From the counted conversion rate and the measured DC current, one can calibrate the *effective gas gain* (gain after losses in charge transfer):

$$\text{gain} = \frac{Q_{\text{conv.}} \cdot f}{I_{\text{anode}}}, \tag{2.2}$$

where f is the conversion rate, and the conversion charge can be estimated:

$$Q_{\text{conv.}} = E_{\text{x-ray}} \sum_i^{\text{comp.}} \frac{x_i}{W_i}. \tag{2.3}$$

Here $E_{\text{x-ray}}$ is the energy of the photon, the sum is over the components of the gas mixture, and x_i and W_i are the volume fraction and average energy spent on one ionization of component i. The W values are gas properties, they depend hardly if at all on the type of radiation, and are typically around twice as large as the lowest ionization potential (few 10 eV). For the gas mixture used throughout this work, Ar/Co_2 70%/30%, the values are $W_{\text{Ar}} = 26.5$ eV and $W_{\text{CO}_2} = 33$ eV [3], and the average $\sum_i^{\text{comp.}} \frac{W_i}{x_i} = 28.5$ eV.

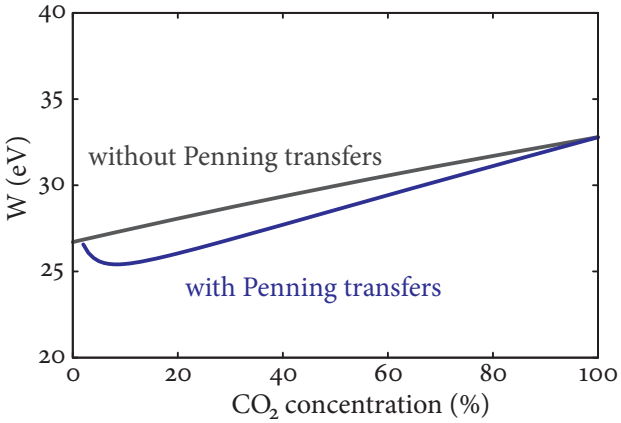

Figure 2.11 — W value of an Ar/CO_2 gas mixture as function of the composition. The straight line is what is predicted by equation 2.3, the curve is simulated with Magboltz (by Heinrich Schindler) using an algorithm that includes the Penning transfer mechanism.

Equation 2.3 is not entirely accurate in that it assumes the components of a gas mixture do not interact with each other. If transfer mechanisms such as the Penning transfer (see section 1.1) are taken into account, the W value for an Ar/CO_2 mixture will be lower, see figure 2.11. A better estimate of the W value for the Ar/CO_2 (70%/30%) mixture is therefore 26.5 eV.

X-ray tubes for soft x-rays have metal targets. These vacuum tubes are made of glass, with beryllium extraction windows. In the tube are only two electrodes: a cathode heating filament and an anode target. The tungsten filament is heated by a current and yields electrons by the *thermionic effect*. The target is at a positive high voltage, and electrons from the filament reaching the target gain a kinetic energy corresponding to that voltage. The voltage should be high enough to excite the relevant emission lines, or even higher to excite them efficiently. K emission lines are the most prominent, especially the K_α line from the transition of an L-electron to the K shell. A side effect of this technique of generating x-rays is *bremsstrahlung*, the photons generated by deceleration and deflection of the electrons from the cathode in the electric field of target nuclei. The spectral distribution of bremsstrahlung from a tube is continuous, contrary to emission lines of the target fluorescence. Many models exist that describe the spectrum of this continuum (for a recent treatment referring to many of these models, see [45]). As a crude approximation, the intensity distribution can be assumed to be proportional to $(E_{max} - E)/E$ (with E the photon energy and E_{max} the maximum photon

energy corresponding to the high voltage on the anode); this appears in each of the models as the dominant factor. The lower end of this energy spectrum is in practice suppressed by absorption, mostly in the tube window. With x-ray tubes high rates of the order of MHz can be achieved even if the beam is collimated to less than a mm^2. Many measurements in this work have been made with a copper x-ray tube operated at 15 kV (E_{max} = 15 keV). For copper, K_α = 8.05 keV [46]. Using equation 2.3 and the (Penning-corrected) average value W = 26.5 eV for our standard gas mixture, this corresponds to 304 electrons per conversion.

Radioactive sources that emit soft x-rays are based on isotopes that decay by *electron capture*, lowering their atomic number by one unit. For example, by far the most commonly used isotope is ^{55}Fe, which decays to ^{55}Mn by capturing a K or L shell electron. This excited Mn atom will emit a K or L photon when it returns to ground state (the L lines are well below a keV and do not penetrate the detector). Again, the K_α line dominates the spectrum: 5.9 keV for Mn [46], corresponding to 211 electrons per conversion in our gas mixture.

A peculiar property of argon-based gas mixtures for x-ray detection is the possibility of part of the x-ray energy to escape. In the process of ionization, argon atoms or ions may get their K level excited, leading to de-excitation by K_α (2.96 keV, 94%) or K_β emission (3.19 keV, 6%) [46]. These energies are just below the argon absorption edge at 3.21 keV, hence the photons have an attenuation length in Ar/CO_2 70%/30% of 4 cm, making it likely for them to escape and get absorbed by the nearest solid. In energy spectra acquired with argon-based gas detectors this effect gives rise to an *escape peak* at an energy of K_α(Ar) lower than the *photopeak*. Such a spectrum (of Cu x-rays) is shown in figure 2.12, measured with a single GEM detector. One may notice a certain skew in the photo peak, this is due to the presence of the Cu K_β line (8.90 keV)), at lower intensity than the K_α. It is possible to suppress this K_β peak with a filter made of nickel, which has an absorption edge at 8.33 keV between Cu K_α and K_β lines, favoring strongly the transmission of the K_α line.

Discharge probability

As mentioned before, discharges are an important issue in micropattern gas detectors. Discharges are primarily caused by high particle rates or highly ionizing particles, both giving rise to high charge densities in the gas. In particle physics experiments highly ionizing particles mostly come from activation of materials due to radiation (neutrons especially). To assess a detector's performance in the presence of highly ionizing particles, a gaseous

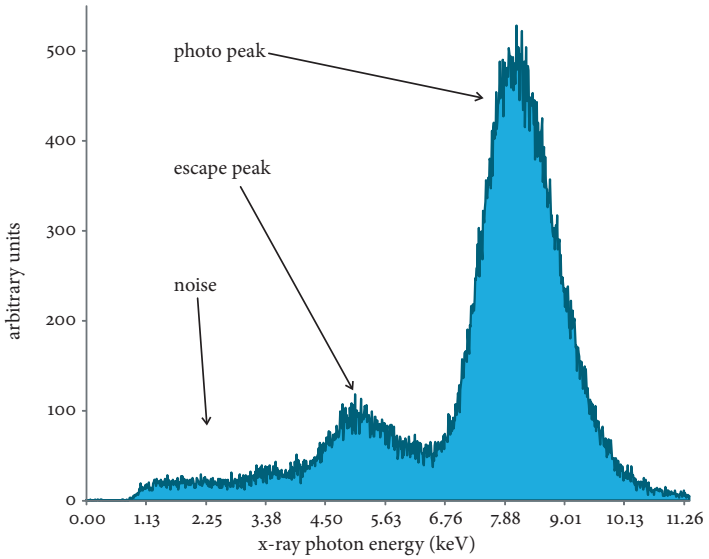

Figure 2.12 — A spectrum of a copper x-ray tube, measured by a single GEM operated at 540 V. The argon escape peak is clearly visible.

α-emitter is used. A piece of tissue[5] containing ^{228}Th is embedded in the gas supply line. ^{228}Th has the following decay chain:

$$
\begin{aligned}
^{228}\mathrm{Th} \rightarrow\ & ^{224}\mathrm{Ra} + \alpha && (5.52\ \mathrm{MeV},\ \text{half life: } 1.9\ \mathrm{y}) \\
\hookrightarrow\ & ^{220}\mathrm{Rn} + \alpha && (5.79\ \mathrm{MeV},\ \text{half life: } 3.6\ \mathrm{d}) \\
\hookrightarrow\ & ^{216}\mathrm{Po} + \alpha && (6.40\ \mathrm{MeV},\ \text{half life: } 56\ \mathrm{s}) \\
\hookrightarrow\ & ^{212}\mathrm{Pb} + \alpha && (6.91\ \mathrm{MeV},\ \text{half life: } 0.15\ \mathrm{s})
\end{aligned}
$$

Radon is a gas, and despite its heavy mass it will be transported to the chamber by the gas flow. Its decay products ^{216}Po and ^{212}Pb have half lives less than a minute, and all three isotopes decay by α-emission of around 6.5 MeV. The α particles mostly hit a solid before they can deposit all their energy in the gas, but still thousands of electron-ion pairs will be created. In this environment the discharge probability can be defined as the ratio of discharge rate to α-decay rate. With a triple GEM detector working at a gain of a few 10^4 (typical for detection of MIPs at full efficiency) the discharge probability measured this way is normally below 10^{-5}. This is exceptionally low, and it is one of the most prominent advantages of triple GEM detectors over every other gas

[5] The piece of tissue is actually a gas mantle for camping gaslights, thorium has a useful candoluminescence spectrum for this purpose.

detector. Below 10^{-5} it becomes increasingly time consuming to measure discharge probability with this method, because of the low α-rate (order of Hz).

Beam tests

Detectors meant for high energy particle physics need to be tested in a high energy particle beam. There the operating conditions are close to those in the final experiment. The most important figure that needs to be found is the *efficiency* (as a function of gain or other hardware settings) for MIPs, this is the probability of detecting a minimum ionizing particle that passes through the detector. As sources available in the lab emit strongly ionizing particles, a beam test is the only way to measure efficiency besides cosmic rays (which have such a low rate that statistics are poor). Also time and position resolution will be different depending on particle type and energy, and if relevant these parameters can also be measured. Pad or strip *multiplicity*, usually as a function of gain, can be found. This can be important for high-rate detectors to estimate the occupancy of the readout channels in the final setup. Furthermore, performance with inclined tracks can be assessed, and in a magnetic field if a magnet is available; in the latter case the Lorentz angle can also be measured (this is a property of the gas mixture).

Chapter Three

LARGE AREA GEMS

This chapter discusses all aspects of the development of large area GEM technology. Attention will be given to challenges in fabrication, handling, assembly and distribution of high voltages. As many applications for large area GEMs foresee large production volumes as well, production strategies and cost development will also be covered. The fabrication technique for large GEMs is well compatible with industrial processing methods, and a cost reduction per unit area of more than an order of magnitude is expected compared to the standard GEM fabrication technique. Finally, a few applications of these new techniques will be discussed.

3.1 Motivation

In 2007 an effort was started to make GEM technology available for large size detectors [37], of the order of a m^2. The primary motivation was the prospect of a tenfold luminosity upgrade of the LHC to SLHC [47]. Various scenarios of such an upgrade are being investigated, with different bunch spacings (options varying from 12.5 to 75 ns). Many detectors in outer tracker stations of the experiments, especially those in the forward regions, will have trouble coping with the increase in particle rate and the potentially even higher increase in occupancy (depending on bunch spacing). These detectors include MWPCs, resistive plate chambers (RPCs) and drift tubes. Several of these will need to be replaced by a detector with higher granularity and a higher rate capability. MPGDs appeared to be a natural option, but these technologies were not yet suitable for the large areas of the detectors they needed to replace.

As mentioned in the previous chapter, the TOTEM experiment includes triple GEM detectors very close to the beam pipe. These detectors are not expected to have difficulty with the increased rate or occupancy of the SLHC. However, the cathode strip chambers (MWPCs) of the T1 subdetector [48] will probably need to be replaced.

In 2008, a prototype large area triple GEM chamber was made, as a candidate for replacing the current TOTEM T1 stations. The active area was $\sim 2000\ cm^2$ and the GEM foils used were 66 cm × 66 cm. To produce foils of such dimensions, limitations in the standard fabrication procedure had to be

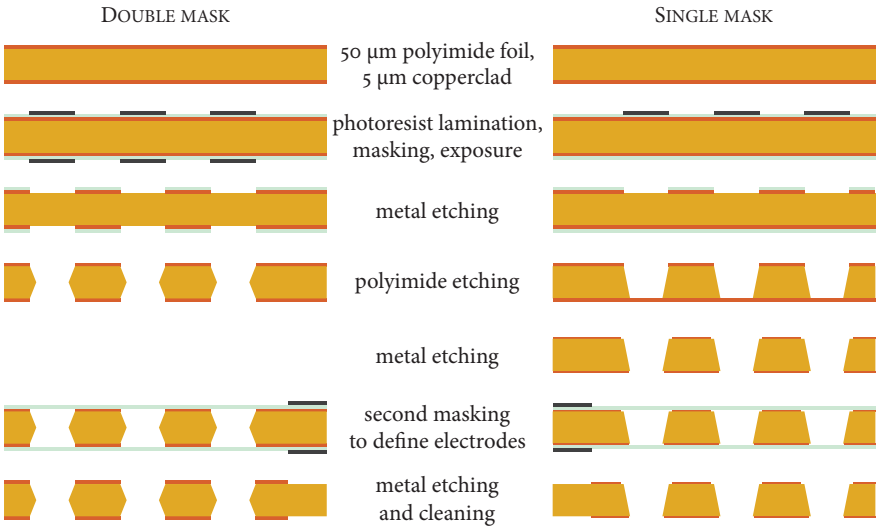

Figure 3.1 — Schematic comparison of procedures for fabrication of a double-mask GEM (left) and a single-mask GEM (right).

overcome. The standard technique for creating the hole pattern, involving accurate alignment of two masks, was replaced by a *single-mask technique*. To exceed the limited width of the base material (typically ~0.5 m) a splicing procedure was developed, as explained in section 3.3. Section 3.4.2 discusses the results that demonstrate the performance of this prototype.

After testing the prototype, and driven by the interest generated by its success, the single-mask technique was further refined. Current single-mask GEMs are visually and in terms of performance hard to distinguish from double-mask GEMs. Several experiments are implementing this technique in their detectors, a few examples are highlighted.

3.2 Single-mask Technique

Production of GEM foils is based on the photolithographic processes commonly employed by the printed circuit industry. The left-hand side of figure 3.1 shows schematically the steps involved in standard GEM fabrication. The GEM hole pattern is transferred by UV-exposure from flexible transparent masks to a copper-clad polyimide foil laminated with a photoresistive material. After development, the foil can be etched in an acid liquid, which removes copper from the holes, but not from where the photoresist still protects the copper. The next step is the etching of the polyimide substrate, for which the holes in

the copper layers act as a mask.

To obtain a homogeneous hole geometry across the foil, it is imperative to keep the alignment error between the top and bottom masks within 5–10 µm. As both the masks and the base material are flexible this alignment is far from trivial, and when foil dimensions exceed about half a meter this method is hardly feasible anymore. A way to overcome this hurdle is shown on the right-hand side of figure 3.1. By using only one mask to pattern only the top copper layer, no alignment needs to be done. The bottom copper layer is etched after the polyimide, using the holes in the polyimide as a mask. The quality and homogeneity of the holes depends now critically on the control of the polyimide etching (which also defines the pattern of the bottom copper layer), where mask alignment used to be the limiting factor.

3.2.1 Polyimide etching

In the development of the single-mask technique, progress has been made in understanding the crucial parameters and conditions of the polyimide etching process. Polyimide etching is done in a basic solution containing ethylene diamine and potassium hydroxide (KOH). The potassium hydroxide has an isotropic etching characteristic, which means that material in contact with the etching liquid is removed at the same rate in all directions. On the other hand, ethylene diamine etches only down into the polyimide (not sideways), but the diameter tapers off as etching proceeds, resulting in conical holes wide on top and narrow at the bottom.

Pure isotropic etching results in holes that are always at least twice as wide as they are deep, and polyimide is removed until far under the electrode, as can be seen in figure 3.2 (foil made by Tech-Etch[1] using a double-mask technique). While the etching under the copper layer leaves irregular cavities in which the electric field is badly defined, the low aspect ratio (defined as the ratio *depth / width* of a hole) really prohibits the use of isotropic etching for a single-mask technique. When etching with a solution of ethylene diamine only, although no material is removed under the copper, the conical edges are not steep enough to arrive at a high aspect ratio. In a solution based on both KOH and ethylene diamine, the steepness of the holes can be modified by controlling the composition of the liquid. The temperature must also be well controlled: raising the temperature increases the etching rate of KOH more than that of ethylene diamine. Furthermore, at temperatures exceeding ~55°C local delaminations between copper and polyimide have been observed,

[1] Tech-Etch Inc., 45 Aldrin Road, Plymouth, MA 02360 USA

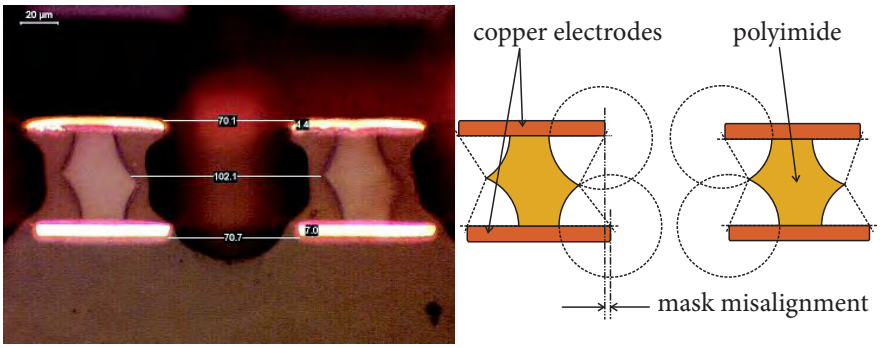

Figure 3.2 — Left: cross-section view of isotropically etched polyimide holes (double-mask technique). The etching extends under the copper electrodes, creating cavities with a circular cross-section, as shown in the reconstruction drawing on the right. GEM foil made by Tech-Etch. The numbers indicate dimensions in microns.

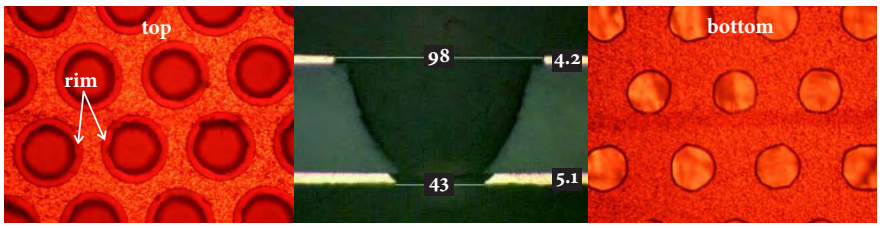

Figure 3.3 — Micrographs of a single-mask GEM foil taken facing the top and bottom electrodes, and a view of the cross-section through the center of a hole. This hole geometry is representative for the GEMs used for the prototype discussed in section 3.4. The numbers are hole diameters and copper thicknesses in microns.

that give rise to irregular etching patterns as the etching liquid flows into the openings created by delamination.

When parameters are optimized one can make holes of ~ 90μm on top, and ~ 45μm on the bottom. This result does not depend critically on one parameter, and can therefore easily and accurately be reproduced with a good uniformity over large areas. Such a hole profile is used for the large area prototype, see the top, cross-section, and bottom micrographs in figure 3.3. The technique described here is patented [51]; significant further improvements developed after finishing the prototype are presented in section 3.5

3.2.2 Copper etching

As shown in figure 3.1, the etching of the top electrode using the single-mask technique is done in the same way as with the double-mask technique. The bottom electrode however, is etched both through the polyimide (which defines the pattern) and from the unprotected outer face of the copper. This is done by immersion of the foil in the acidic etchant, without applying direct current (electrolytic etching), and without physical protection in the form of a photoresist layer on any of the electrodes. Therefore both electrodes will be etched at the same time, and at the same rate. In the etching process the electrodes are slimmed to less than half their original thickness. Also, as the copper etching process is isotropic, a clearance arises around the edge of the hole in the polyimide. This is visible in the right panel of figure 3.4.

This clearance, usually referred to as the *rim*, is known to degrade the time stability of the gain due to dielectric surface charging. To minimize the width of the rim, the thickness of the electrodes can already be minimized before etching the holes. Slimming down GEM electrodes was shown in [49] to leave the detector properties unaffected, only reducing the material budget significantly. In [49] a microetch liquid based on ammonium persulfate was used. This type of liquid etches more efficiently at grain boundaries, giving the copper surface a matte look. Using this surface etchant on large areas, we found that the resulting copper thickness varies by a few microns across the foil. With the single-mask technique, this causes some variation in hole diameter on the bottom electrodes, which gives rise to gain inhomogeneities. In addition, the increased surface roughness degrades the definition of the holes in the bottom. Such rough copper edges around the hole may cause discharges during GEM operation.

By using chromic acid instead of a microetch as a surface etchant, both issues of inhomogeneity and surface roughness are overcome, leaving a shiny surface. Figure 3.4 compares two bottom electrodes etched with one liquid and the other. In the sample shown on the right, the etching process was stopped so soon after the holes in the bottom were opened, that the edge of the metal is still very sharp. This is a natural consequence of the isotropic etching through the hole in the polyimide, and can typically be solved by moderate over-etching. Chromic acid has now completely replaced the microetch as a surface etchant for large area foils.

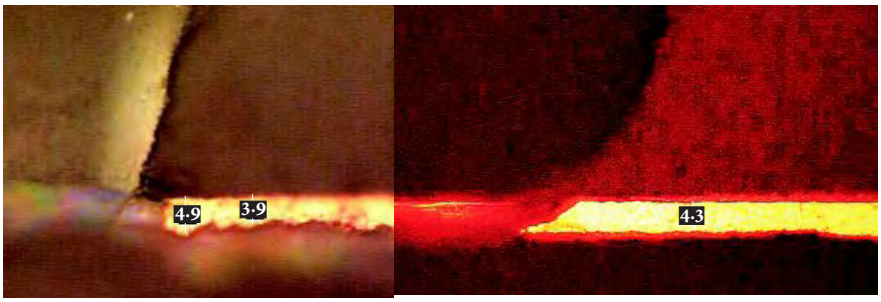

Figure 3.4 — High magnification cross section views of copper layers on GEMs, at the bottom edge of the hole. Both samples were etched on the surface, to modify the thickness of the layer. For the left sample, a microetch based on ammonium persulfate was used, the right sample was etched with chromic acid.

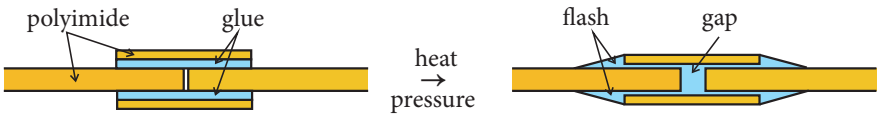

Figure 3.5 — The principle of splicing GEM foils with slim strips of coverlayer. When the adhesive is cured, the heat makes it somewhat liquid so that it can migrate and maximize contact surface. The pressure exerted at the same time squeezes some glue out from underneath the coverlayer, and causes the glue inside the gap between the foils to expel the foils and widen the gap.

3.3 GEM splicing

Although the single-mask technique allows patterning foils of virtually any size, there are still limits on the dimensions of the base material. Double sided (adhesiveless) copper-clad polyimide is available from rolls of around half a meter wide. This width varies only minimally between suppliers, the widest on offer is 24″ (61 cm).

A method was developed to splice foils together with a narrow seam, using a flexible polyimide coverlayer[2]. Coverlayers are commonly used in the PCB industry to protect flexible printed circuits without losing their flexibility. The coverlayer used here consists of a 25 µm thick Kapton HN substrate, covered on one side with an adhesive. The simple procedure is illustrated in figure 3.5. The glue of the coverlayer is a B-staged (semi-cured) acrylic adhesive, which

[2]The material used throughout this work is Pyralux LF0110 Coverlay, from DuPont.

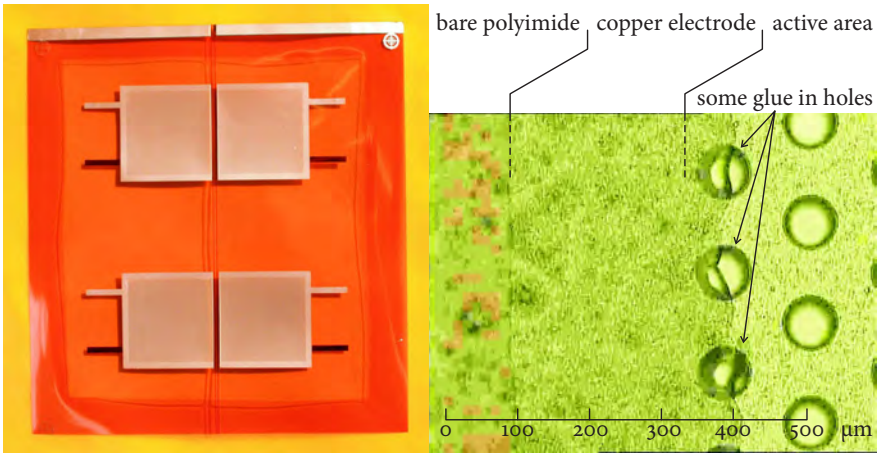

Figure 3.6 — Left: two pairs of 3 cm × 3 cm GEM foils glued together, to validate the splicing method. The right panel is a micrograph of the same sample showing that at some places the glue of the coverlayer entered a few of the GEM holes.

polymerizes during a heat cure. The coverlayer has mechanical, thermal and dielectrical properties that are compatible with those of the GEM foils.

3.3.1 Splicing test

This method results in narrow, flat and strong seams that can be framed like normal foils. To test how GEMs perform after applying this method, we spliced two pairs of 3 cm × 3 cm GEMs together, see figure 3.6. A counting rate scan over the seam of one of these glued pairs is shown in Figure 3.7. This can be regarded as a measure of the efficiency of the GEM for detecting 8.05 keV x-ray conversions in the drift region, which is 100% in normal conditions. From figure 3.7 it is clear that the efficiency is normal until above the seam. Note that a collimator of 0.5 mm diameter was used on the x-ray source which makes the inefficient area look wider than the seam. In the background a microscope image of a seam is also shown, scaled to the horizontal axis of the plot.

The high pressure exerted by a standard PCB heat-press, typically ~ 20 bar, causes migration of the adhesive, resulting in a flash left and right of the seam. The right panel of figure 3.6 shows that some of the glue actually reached the active area and filled a few of the GEM holes (the dielectric strength and leakage current of this GEM were however not affected by this). Furthermore, this pressure tends to expel the two foils (with a force of ~ 1 N per cm of seam

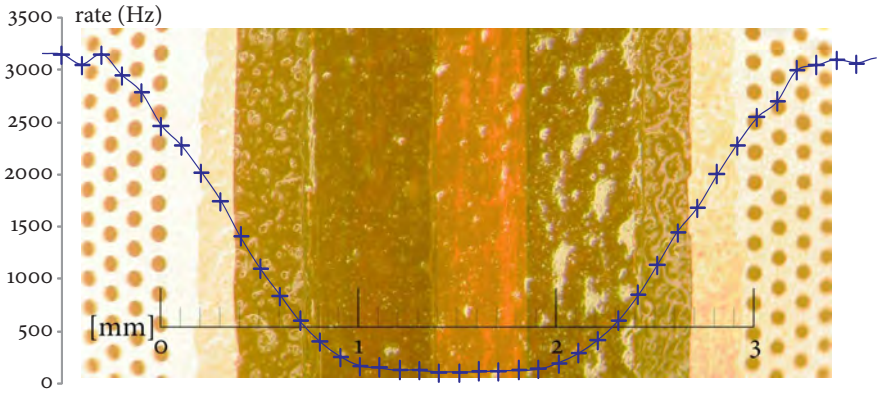

Figure 3.7 — A counting rate scan over the seam of two spliced GEM foils. The measurement was taken with a copper x-ray source with a ∅ 0.5 mm collimator.

length), leaving a glue-filled gap in the middle. These effects are indicated in figure 3.5, and clearly visible in figure 3.7. Tests show that the effective widening of the seam by these effects can be eliminated by adjusting the pressure exerted while curing the adhesive. Optimizing this process one can reduce the width of the seam to ~2 mm.

3.3.2 *Tooling*

This splicing technique was used to make the prototype presented in the next section, of which the dimensions exceeded the available base material. A tool was designed to make the splices without putting pressure also on the entire active area. It is based on an old bending tool for steel sheets, with the blade replaced by a blunt-edged copper plate to press the seam while being heated by high-power resistors mounted all over the copper plate. A feedback unit constrains temperature excursions to few degrees.

Although the splicing of large GEM foils in this way was rather successful it also required quite some skill, and more advanced tooling will be needed for larger scale production. Also, spliced foils are not as easy to stretch as plain foils, because the coverlayer modifies the elastic properties of the material locally.

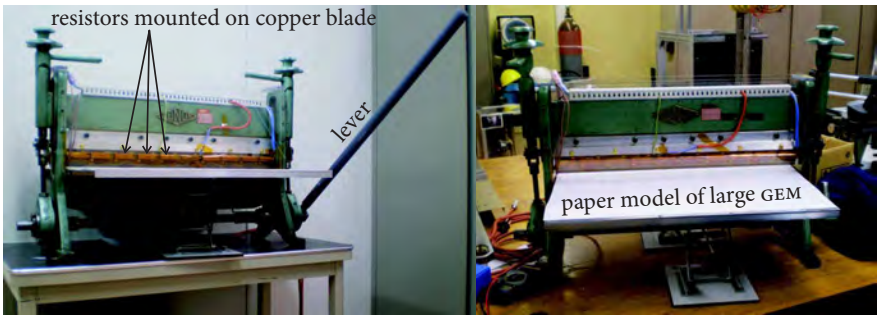

Figure 3.8 — A modified steel-bending machine serves as a heat-press for splicing GEM foils. It is here fitted with a 1:1 paper model of the GEMs used for the large area prototype.

3.4 A FULL SCALE PROTOTYPE

Based on the techniques described above, we built a prototype large area triple GEM detector. It has an area of ~ 2000 cm², and is based on foils of 66 × 66 cm². This prototype is aimed for application in the TOTEM experiment, as a replacement of the T1 subdetector. Figure 3.9 shows how a disc with adjustable radius can be made of ten such chambers. The overlap of the chambers on both sides of a disc ensures complete coverage, and allows for alignment. With six such discs one can build a telescope similar to the current T1.

The prototype chamber uses a triple GEM configuration with a pad readout. Figure 3.10 shows the finished prototype and the layout of the GEM foils. The two half single-mask foils were spliced in the middle, with the method described above. The edges of the foils and the alignment holes were etched in the same process as the GEM holes, to ensure perfect alignment and straightness. To reduce the energy deposited when a discharge occurs [13], the top electrodes are segmented and each segment is connected via a 10 MΩ resistor, as described in previous chapter.

Figure 3.11 shows how the prototype is built up, and how the GEM foils connect to the high voltage distributor. The readout board is a two-layer printed circuit board, on a substrate of 200 µm FR4. There are 1024 readout pads on the top layer, varying in area from 0.25 cm² to 6 cm². The traces connecting these pads to the readout electronics are on the bottom layer. This readout configuration is not optimized for the experimental application, but rather for simplicity, cost and ease of manufacturing. VFAT readout chips are

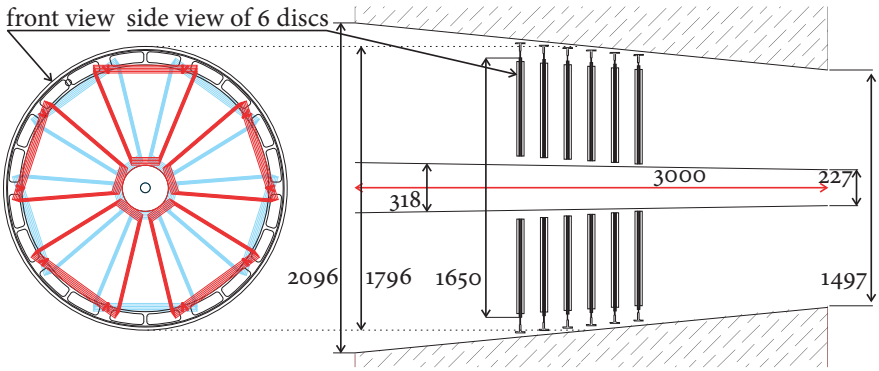

Figure 3.9 — An idea for replacement of the current TOTEM T1 cathode strip chambers with large area GEM detectors. Discs of adjustable radius are built from 2 × 5 chambers in a back-to-back arrangement (the ones indicated in red are mounted on the front of the disc, the blue ones on the back). To the right is how six such discs could be installed in the T1 envelope in the CMS detector.

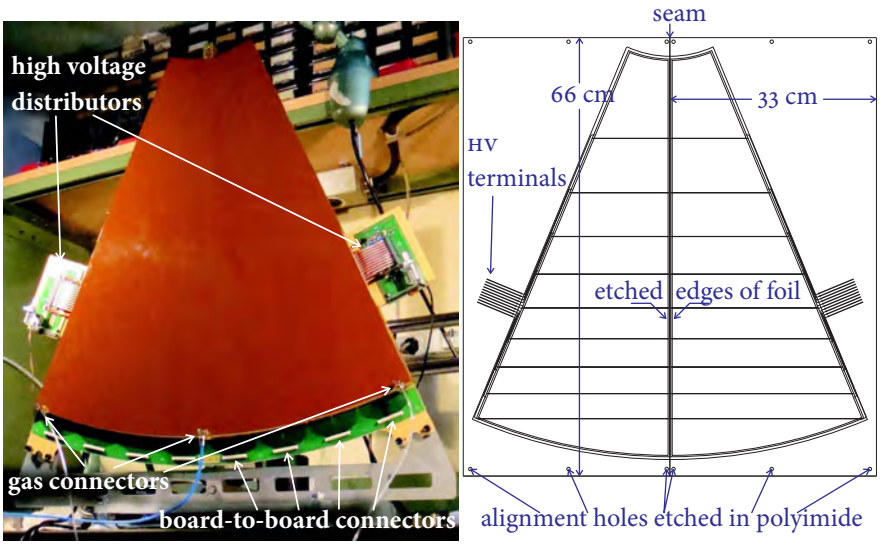

Figure 3.10 — The large prototype mounted on its support (left) and the layout of the GEM foils used for it (right). The top electrodes are divided in sectors of ≤ 100 cm² to keep the capacitance per sector below 5 nF.

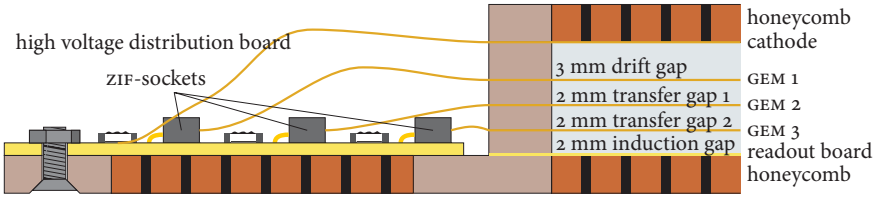

Figure 3.11 — Schematic buildup of the chamber.

directly wire-bonded to small hybrid PCBs, which connect to the detector via 130-pin board-to-board connectors. These electronics were developed for all subdetectors of TOTEM, with variants optimized for gaseous detectors (cathode strip chambers and GEMs) or silicon strip sensors (roman pots). The prototype has also been read out by Gassiplex [52] electronics (developed from the original GASPLEX chip [53]) and by a single-channel amplifier reading a number of pads connected together.

3.4.1 *High voltage distribution*

The segmented top electrodes of each GEM foil are connected to the high voltage distributor via traces that run along the edges of the foil. When spacer frames are glued to the stretched foils these traces are embedded in the frames. In this way, the high voltage distribution board can be made compact, which makes it easier to screen, less vulnerable to pickup, and safer.

ZIF connectors

To make the connections with the board, so called zero-insertion-force (ZIF) sockets[3] were used, rather than hand soldering the terminals to the board, see figure 3.12. ZIF sockets are intended to connect flexible to rigid printed circuits. The flexible circuit needs no plug or pins to be fitted, but enters the socket freely with exposed copper terminals aligned with the pins of the socket. Then a latch of the socket is closed, which clamps the inserted flexible circuit, thereby both keeping it in place and establishing reliable contacts. These connectors have much finer pin spacings (0.5 mm in our case) than one would normally use for high voltage purposes, but by connecting groups of pins together and leaving pins floating between these groups, isolation between channels is several kV (validated up to 4 kV, no arcs observed) and alignment of the strips in the socket is not critical. This can save a lot of hand

[3] We used two types: FH28H-80S-0.5SH (80-pins) and FH12-06S-0.5SH (6-pins), both of Hirose. The former for the 10-terminal strips to the top sectors, and the latter for the single terminal strips to the bottom electrodes, including the cathode.

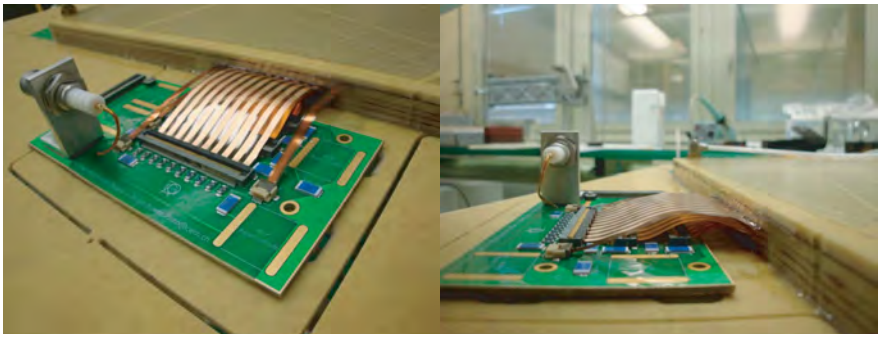

Figure 3.12 — A compact high voltage divider board, using ZIF sockets to connect to the terminal strips of the GEM foils.

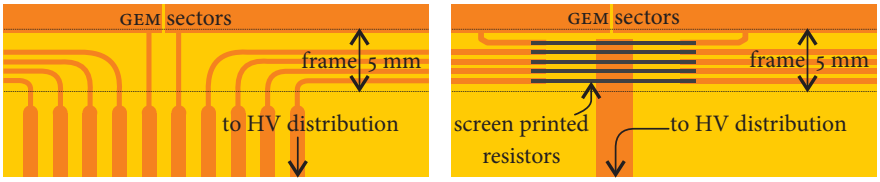

Figure 3.13 — Two methods to connect GEM foils to the high voltage circuitry. On the left the method applied in the prototype, with traces that connect to the sectors embedded in the frame. On the right a method that is still under study, where the safety resistors are screen printed on the foil, and can therefore also be embedded in the frame.

work when the area (and therefore the number of sectors) is large. Moreover, using these sockets one can easily replace, debug or modify boards.

Printed resistors

An even more compact solution for high voltage distribution, still under study, would be to embed not only the routing but also the safety resistors in the frame. This would be possible by screen printing polymer thick film (PTF) resistors on the foil in an area that will be covered by a frame. Figure 3.13 illustrates this method, and compares it to the method currently used. This method could simplify high voltage circuitry of large area GEM detectors considerably. As these resistors are not part of the voltage divider chain and are not supposed to carry any appreciable current (the leakage current of one sector is typically ~ 1 nA), the requirements for these resistors are extremely low.

However, it proved difficult to find reliable PTF materials of such high

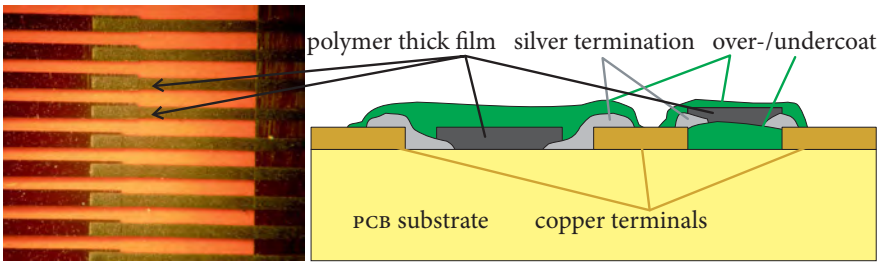

Figure 3.14 — Left: PTF resistors, screen printed on a test pattern. Right: suggested improvements to the straightforward single-layer printing of resistors on a circuit.

resistivity (we aim for resistance values of 10 MΩ), especially if they have to be cured on a polyimide substrate. Screen printing such resistors was tested with a paste[4] that had a nominal value of 1 MΩ/□ if printed in conditions according to the instructions. The paste was applied to a test pattern with one grounded central contact and individual terminals to which a voltage could be applied with a test probe, a detail of this circuit is shown to the left of figure 3.14. All resistors printed on this pattern had an aspect ratio of 1:10 to obtain a resistance of 10 MΩ; the width of the resistors varied from 150 to 500 µm (the detail in the figure shows 500 and 450 µm resistors). The pattern was made on the same base material as GEMs are made of, to simulate the relevant conditions. The size of this pattern was within 10 × 10 cm² so that it could be framed like a standard size GEM foil, to check the possible damage done to the brittle resistive body during stretching.

Results were however disappointing, with resistance values several orders of magnitude too high. The right side of figure 3.14 shows various possible configurations in which resistive pastes can be applied. A silver paste can be used to improve contact resistance between the resistive paste and metal terminal, this is normally not very important if a high resistance value is desired. A so-called undercoat of epoxy can be applied to prevent the substrate from absorbing liquid parts of the uncured paste. An overcoat can protect the resistive body from mechanical damage as a consequence of scratching the surface or bending the substrate. Figure 3.15 shows several trials of such additional layers applied to the test pattern mentioned above. Despite the good quality and alignment of the printing, none of these techniques caused any notable change of performance. One test of the same pattern on a rigid FR4 substrate (shown in the rightmost panel of figure 3.15) gave much better results,

[4] Tu-1M-8 from Asahi Chemical Laboratory.

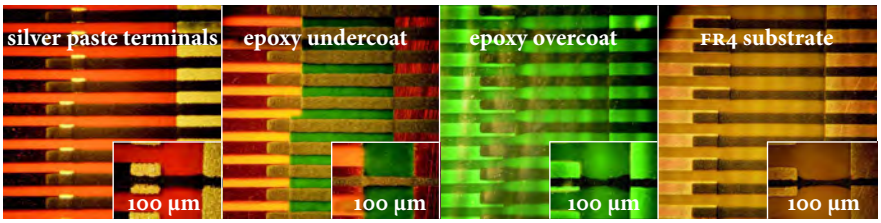

Figure 3.15 — Several tests of screen printing PTF resistors, with or without some of the layers suggested in figure 3.14. The main panels show the widest resistors on the test pattern (500 and 450 µm), while the inset shows one of the thinnest (150 µm). The rightmost panel shows a simple print of PTF on the same test pattern on an FR4 substrate (instead of polyimide).

indicating that the polyimide substrate was probably the main problem.

An alternative method to apply resistors to an insulating substrate is by spraying. This could perhaps give better results, but spraying seems not very attractive on a delicate GEM, where the slightest contamination in the holes could make an entire foil unusable. The resistive pastes used to make most discrete high voltage resistors have a much better quality, but those are cured at temperatures around 800°C on ceramic substrates. The idea of using printed resistors for the high voltage distribution of large area GEMs is attractive, but it has been shelved for as long as no reliable resistive pastes are available.

3.4.2 Performance

Measurements done during development of the single-mask technique, of small samples (10 cm × 10 cm) of single-mask GEMs have shown a performance similar to standard GEMs in terms of gain stability and homogeneity, energy resolution, rate capability, discharge tolerance, and reproducibility. Figure 3.16 shows the gain characteristics of several single-mask GEMs, and for comparison a double-mask GEM. All curves were acquired in a single GEM configuration. Clearly, the single-mask foils need some 50 V more to obtain similar gain. However, their discharge limit is also higher, and typically the maximum working gain is similar (few thousand for a single GEM). The higher voltage needed for the single-mask samples is attributed to the wider holes in these productions, see figure 3.3.

Tests with the prototype showed performance consistent with these small area foils. Its energy resolution was measured with copper x-rays (8.05 keV) to be 9.5% RMS (22.4% FWHM), see figure 3.17. More details on how these tests

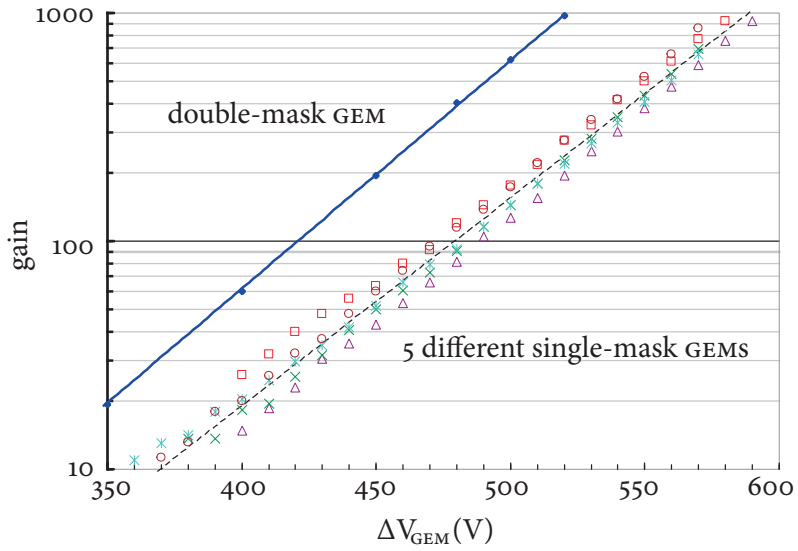

Figure 3.16 — Gain vs. voltage curves for several 10 cm × 10 cm foils of single-mask GEMs and one double-mask GEM.

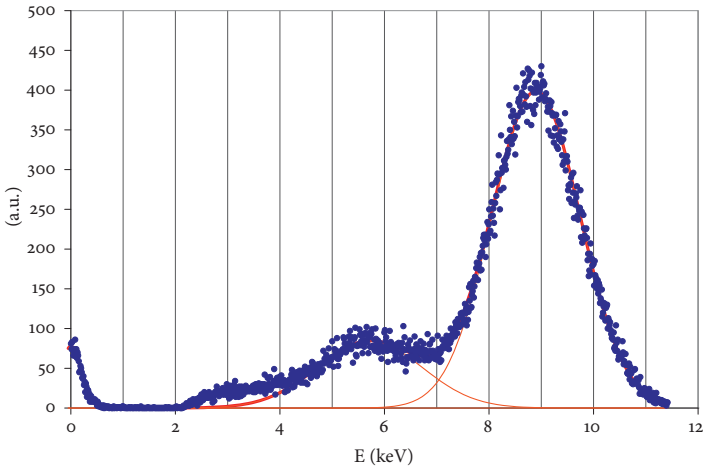

Figure 3.17 — A pulse height spectrum of copper x-ray conversions in argon/CO_2 gas mixture, measured with the large prototype .

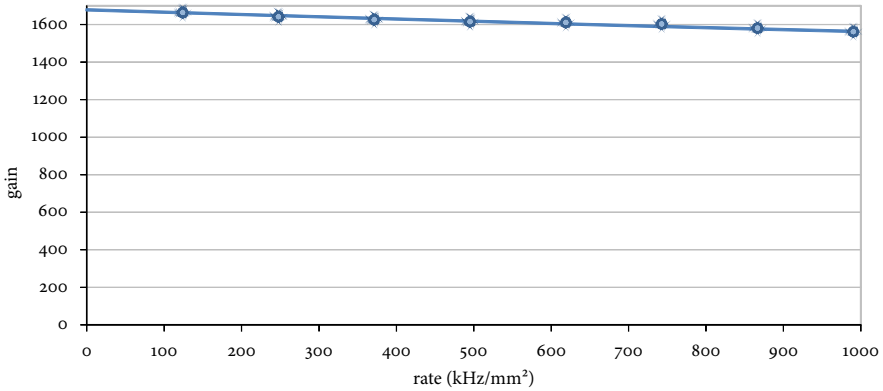

Figure 3.18 — Effective gain vs. rate of copper x-ray conversions in a single-mask triple GEM arrangement. In a gas mixture of argon with 30% carbon dioxide, each conversion releases about 304 primary electrons (see previous chapter). In this measurement, a ∅1.5 mm collimator was used, and the anode current of the chamber went up to 560 nA. The curve is a fit of a function $G = Ae^{c(V_{\text{GEM1}}+V_{\text{GEM2}}+V_{\text{GEM3}}+sI_aR_s)}$, where the constants A, c are known from fits of the gain curves shown in figure 3.16; I_a is the anode current measured here; $R_s = 10M\Omega$ is the value of the safety resistor introduced in previous chapter; s is the fit parameter. The downward trend is due to the high current through the last GEM that gives rise to a voltage drop $\Delta V = I_{\text{GEM3}}R_s$ over the 10 MΩ safety resistor. The GEM current is assumed to be proportional to the anode current: $I_{\text{GEM3}} = sI_a$.

are done are given in section 2.3. The rate capability of these foils in triple GEM configuration was tested with a copper x-ray tube, with which the rate could be tuned over a wide range. The result is shown in figure 3.18 as the effective gain as function of rate; the gain was established by measuring the anode current. The gain is hardly affected by a rate that exceeds any practical application. During this test we also observed an initial gain loss (at the lowest rate) of about 30% due to charging up of the dielectric. However, no rate dependence of this effect was found throughout the range of the measurement, and the stabilization time constant was only 25 seconds.

The prototype has been tested in pion beams of the SPS at CERN. The latest such test was done by members of the TOTEM collaboration, interested in adopting such chambers in their T1 telescope. Figures 3.19 and 3.20 show a few of the results: efficiency curves reaching >99% efficiency and efficiency scatter plots revealing design features of the detector.

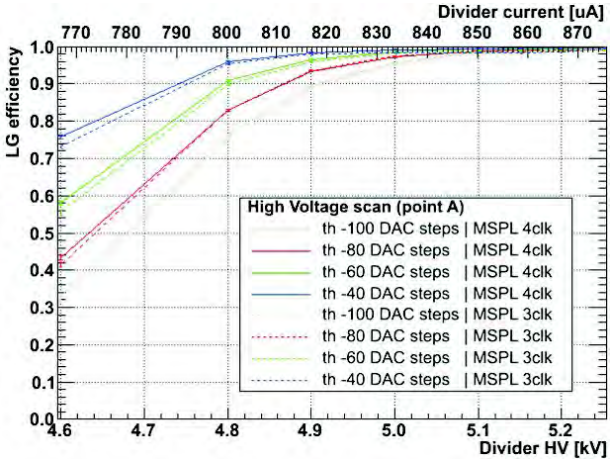

Figure 3.19 — Efficiency curves measured with a 150 GeV pion beam. The different curves correspond to different settings of the threshold and of the monostable oscillator of the VFAT front-end electronics used to read out the prototype. [54]

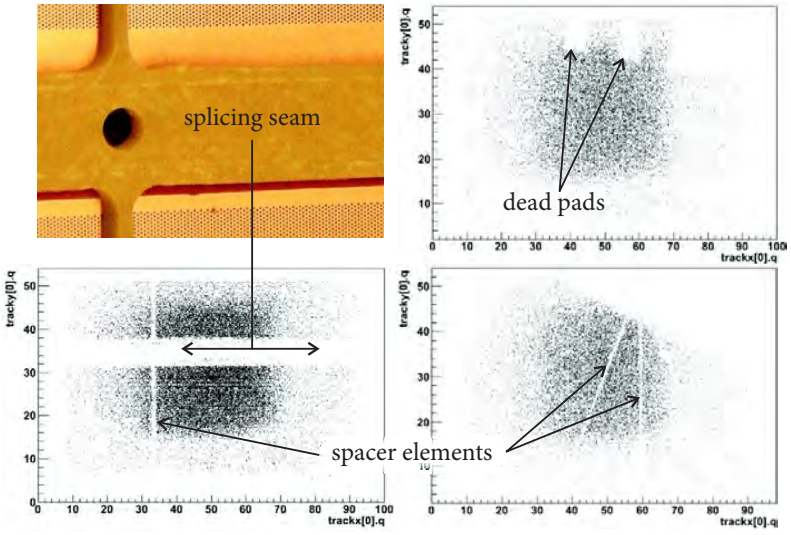

Figure 3.20 — Some efficiency scatter plots of various locations of the prototype. One clearly recognizes the features of spacers, the splicing seam, and the pad layout where apparently some pads had a connection problem or the electronics had dead channels. [54]

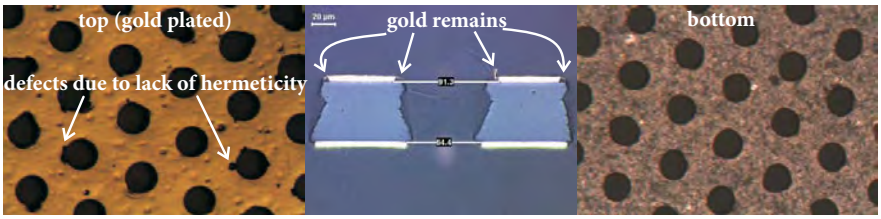

Figure 3.21 — Galvanic protection by a very thin gold layer over the top electrode. Due to failing hermeticity of the layer, some copper is etched underneath it.

3.5 Refinement of single-mask technique

After the prototype was finished, efforts continued to engineer hole profiles such that single-mask GEMs have gain curves compatible with double-mask GEMs and minimal charging-up. This development of the single-mask technique ended in a hole shape that can hardly be distinguished from a double-mask GEM.

Initially, the attention was focused on reducing or eliminating the rim (see section 3.2.2). In order to avoid creating the rim in the top electrode completely, one has to protect the metal when etching the bottom electrode. This can roughly be done in two ways: *galvanic protection* and *electrochemical protection*.

Galvanic protection

With galvanic protection, the top electrode is hermetically covered by a layer that is not attacked by the etchant. A few tests have been done using gold as protection layer. It was suggested that a tin layer may work as well, with the added benefit of lower cost and the possibility to remove the layer afterwards. However, it turns out to be quite difficult to obtain a good hermeticity, and also the slightest delamination between copper and polyimide leads to a leak through which the etchant can attack the copper, see figure 3.21. Due to the dents in the edge of the electrode around the hole, indicated in the figure, these foils tend to spark already at fairly low voltage. It is therefore difficult to reach sufficient gain for practical applications.

Electrochemical protection

Electrochemical protection proved to be more successful in avoiding a rim on the top electrode, see figure 3.22. It works by giving the top electrode a few volts negative potential with respect to the bottom electrode and the walls of the etching bath. The top electrode then becomes inert to the reactions that attack the bottom electrode. This is essentially different from electrolytic

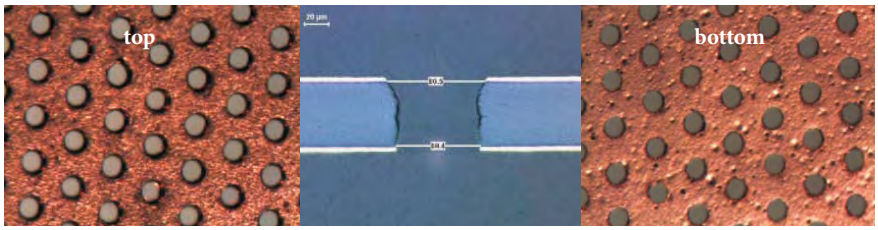

Figure 3.22 — Chemical protection of the top electrode. After etching the bottom electrode, a final short polyimide etching gets rid of the bottom rim, and makes the hole almost cylindrical.

etching[5], where a direct current flows from the metal to be etched (i.e. the bottom electrode) to an external electrode. With electrochemical protection a direct current runs from the external electrode to the top electrode.

The GEMs made this way have a gain almost consistent with standard GEMs, and are more stable than those shown in figure 3.3. However, they seem to be more easily damaged by discharges than other GEMs; a single discharge can make a conductive contact (< 1MΩ) between top and bottom electrodes. Adding a rim of about 1–2 µm can solve this issue.

2nd polyimide etching

A final and crucial improvement comes with the introduction of a second polyimide etching stage, after the holes in top and bottom electrodes are finished. Optimally, the holes in the bottom electrode are etched until they have the same diameter as those in the top electrode. This can be safely done as long as the top electrode is being protected electrochemically against the etchant. When after this copper etching phase the foil is again immersed in a polyimide etching liquid, a biconical hole shape is obtained very similar to double-mask GEMs, see figure 3.23. This is shown in figure 3.23, which complements the basic fabrication scheme from figure 3.1. This shape is consistent from foil to foil and from one production to another, and also very large foils (~ 100 × 45 cm²) have been made reliably. These GEMs behave in all respects similar to double-mask GEMs. The last polyimide etching phase goes a long way toward restoring the top-bottom symmetry, so that flipping a foil has only a minor effect on its gain behavior.

[5] Electrolytic etching had been suggested as a way to etch the holes in the bottom electrode. Results were consistently poor however, and this method was abandoned.

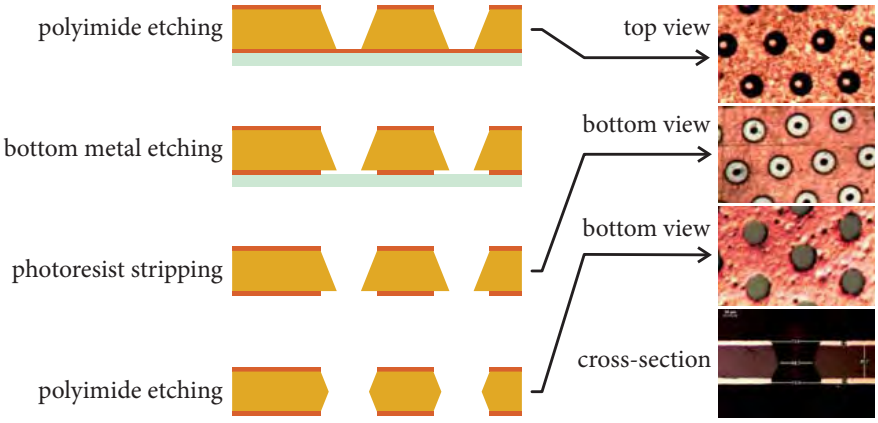

Figure 3.23 — After a final second polyimide etching phase the holes become biconical and very similar to double mask GEMs.

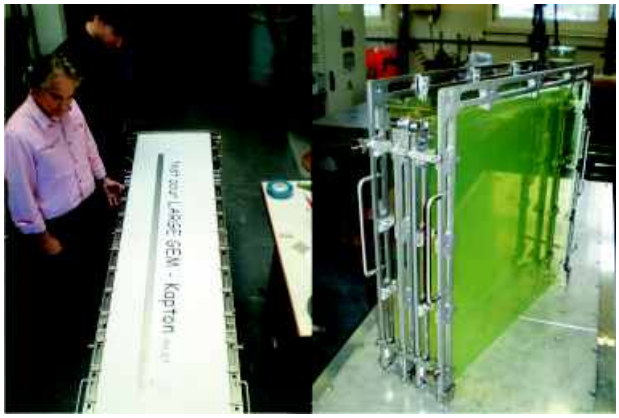

Figure 3.24 — Stainless steel portfolio for handling GEMs of up to 0.5 × 2 m² during fabrication. Left in the opened state, as it will be when a foil is mounted or dismounted. Right in the folded state, as it will be when it is moved or immersed in chemistry.

3.6 Production

The large area prototype generated a lot of interest in large area GEMs. Applications range from forward tracking and triggering in SLHC experiments (CMS, TOTEM), to barrel tracking with cylindrical GEMs [55], digital hadronic calorimetry for ILC experiments [56], cosmic muon tomography for detection of high Z materials [40], time projection chamber readout [31], and various tracking detectors for nuclear physics experiments.

In the fabrication of ever larger GEMs, handling is a growing concern. Moving large and fragile foils from one bath to another is not trivial, and the baths themselves also have finite dimensions. A foldable portfolio was designed to solve this problem, see figure 3.24. It is made of stainless steel, with no plastic components or lubricants, so that it can be immersed in the etching liquids together with the foil it holds. This opens the way for fabrication of foils of up to $0.5 \times 2\ m^2$ in the DEM workshop at CERN.

For many of the applications mentioned above, the production volumes foreseen are much larger than for the standard GEM detectors made thus far. Therefore, some industrialization of production is foreseen. Contrary to standard GEMs, single-mask GEMs are particularly well suited for mass production. All steps in the fabrication process can in principle be done with roll-to-roll equipment, due to the absence of manual interventions (i.e. the alignment of films for each foil separately). This means that some or all of the steps can be subcontracted to external companies, and the GEMs can be transported on their rolls (100 meters long). The maximum production rate using roll-to-roll equipment is several thousand m^2 per month, much greater than required for detector development. The price per unit area is expected to drop by almost two orders of magnitude compared to standard GEMs.

Assembly without stretching

One concern that rises with large production volumes is that the procedures for stretching and framing GEMs (described in section 2.2.2) will become the bottleneck in the production of large numbers of detectors. One possible solution to this issue would be to use spacers with many more thin elements inside the active area. In that case no mechanical tension is needed to keep a uniform spacing between foils. The first material that comes to mind for such a spacer is the Nomex honeycomb already widely used to make the backings of the cathode and readout board. Tests in the lab have been done with a

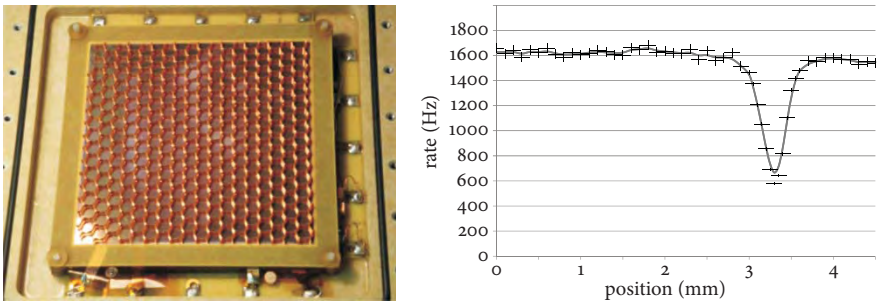

Figure 3.25 — Left: a small prototype chamber using Nomex honeycomb material as spacers. Right: x-ray counting rate scan over part of the active area of the detector on the left. The dip is due to charge absorption by a spacer element.

$10 \times 10\,\mathrm{cm}^2$ prototype fitted with standard Nomex honeycombs with 6.5 mm cell spacing, see figure 3.25. So far the results indicate that the detector functions without any problems of stability, but with a severe loss of efficiency. Due to diffusion of drifting electrodes, the effective width of a spacer element is many times greater than its measured physical thickness of ~ 15 µm. This is clear from the plot on the right of figure 3.25, which shows an x-ray rate scan across part of the active area of the detector shown on the left. Although the rate never drops to zero (the x-ray collimator had a diameter of 0.2 mm, wider than the honeycomb spacer material), the total width of the dip is about 0.8 mm. This is only because of charge losses due to diffusion.

The damage to the efficiency could be reduced by using a wider cell spacing, reduced transfer gaps, or a low diffusion gas mixture. A beam test was done with honeycombs with a wider cell spacing of 12 mm, one of the widest delivered by industrial suppliers. Figure 3.26 shows a hit map from this beam test, where the shadow of a honeycomb is clearly visible. This shadow is again very wide compared to the the actual thickness of the spacer elements, and the degradation of efficiency is obvious. During this beam test efficiencies of around 70% were reconstructed for this chamber. Although this result was discouraging, efforts are continuing to validate and optimize this method for use in applications where cost and ease of production may be more important than the highest efficiency.

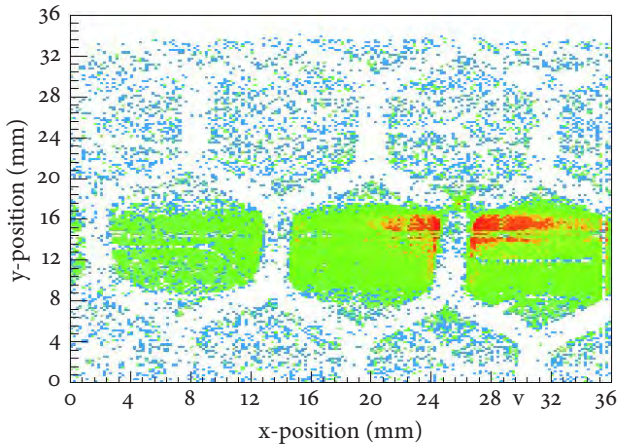

Figure 3.26 — A hit map of one SPS spill acquired during a beam test [57]. The triple-GEM detector had Nomex honeycombs of 12 mm cell spacing in all gaps. The honeycomb pattern that is visible is presumably the shadow of the honeycomb in the drift gap, which is most crucial for the efficiency.

3.7 Conclusion

Large area GEM technology has moved rapidly from an R&D study to applications in research and beyond. Single-mask GEM foils can be made at any desirable length, and their performance is now very similar to traditional GEMs. The splicing of GEM foils in order to obtain GEMs that are both long and wide has been validated, but the complicated production and assembly may make it unsuitable for larger productions.

At the time of writing these techniques have only been applied to prototypes. Once the groups involved start with the production of detectors for their applications it will become clear if single-mask GEMs fulfill their promise of cost reduction by orders of magnitude. Especially the efforts of high-profile applications such as CMS will give the technology a lot of visibility, and will help disseminating it further.

Chapter Four

SPHERICAL GEMS

4.1 Parallax error

The development of spherical GEMs is aimed at eliminating the *parallax error* in detection of neutral radiation (photons or neutrons) coming from a point-like source. This error arises from the uncertainty of how deep radiation penetrates the sensitive volume before causing ionization (given that a gaseous component acts as a converter from neutral radiation to ionization). Figure 4.1 shows that the depth of interaction of x-rays and thermal neutrons in a gas volume ranges from a few to many millimeters, even when using the most efficient gases known for these purposes. The situation is similar for gaseous VUV photoconverters such as tetrakis dimethylamine ethylene (TMAE) or triethylamine (TEA) [59]. If the electric field in the conversion region of a gas detector is not parallel to the direction of irradiation, an uncertain conversion depth will give rise to an error in position reconstruction, see Fig. 4.2.

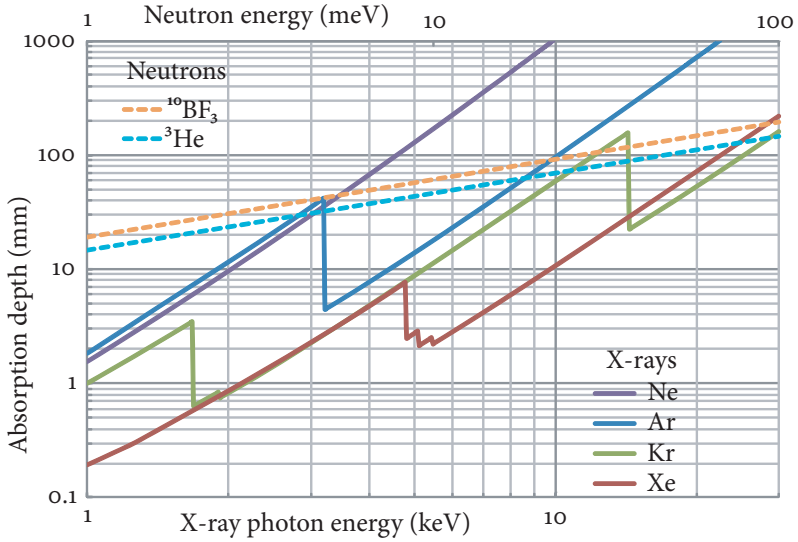

Figure 4.1 — Absorption length of various x-ray and thermal neutron conversion gases at atmospheric pressure, as a function of the energy of x-ray photons (lower horizontal scale) or neutrons (upper scale). Calculated from cross-section data [58, 6].

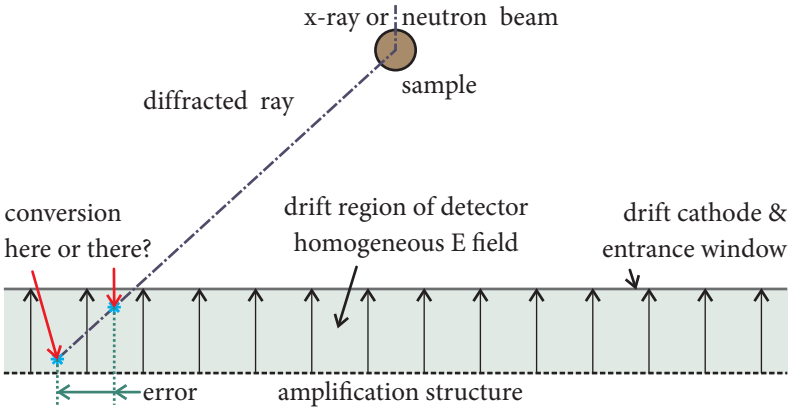

Figure 4.2 — The cause of a parallax error in a gas detector with a homogeneous drift field.

Methods that have previously been used to suppress parallax error include:

- Arranging small area flat detectors in such positions as to approximate a spherical shape [60].
- Creating an almost spherical conversion region with foils and meshes, then transferring the charge to a planar wire chamber [61, 62].
- Having a spherical cathode with an otherwise flat detector, while reducing the conversion depth by using an efficient conversion gas at a high pressure (~ 3 bar) [63, 64].
- Imitating a spherical cathode by dividing a flat electrode into concentric circular segments and controlling the voltage applied to each sector with a resistive divider [65].
- Using a pulsed radiation source or additional hardware to calculate the depth of interaction per event, then correct the position reconstruction [66].

Each of these methods has its limitations. In all cases the challenge of making a fully spherical detector, however desirable, is avoided.

With a spherical GEM and a spherical cathode one can build a detector with a truly radial electric field in the conversion gap, thus eliminating the parallax error. We developed methods to make spherical GEMs, curved spacers and a conical field cage. These methods will be discussed in detail. First tests

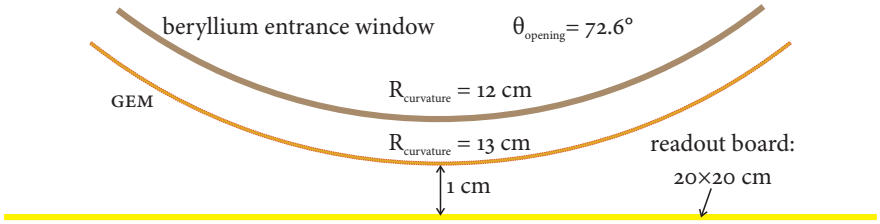

Figure 4.3 — Testing configuration of spherical GEM in a chamber with a spherical beryllium entrance window and a flat readout.

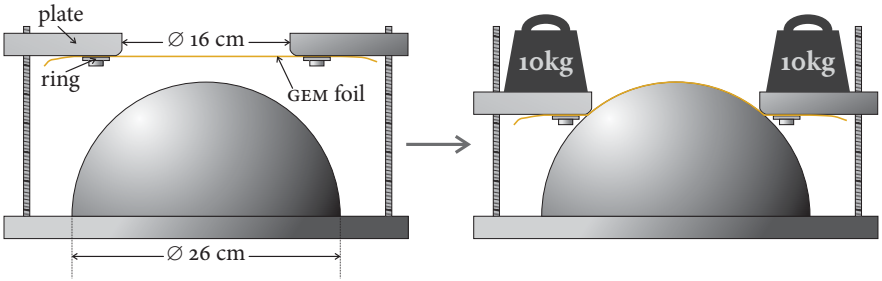

Figure 4.4 — The setup built to spherically form a flat GEM. The setup is placed in a vacuum vessel inside an oven. All parts are stainless steel.

of an assembly of these components were done in an existing detector with a spherical beryllium entrance window, see Fig. 4.3.

4.2 Manufacturing

For the manufacturing of a spherical GEM we start with a flat GEM foil. The shape of the electrodes is designed for the purpose; otherwise the foils used are no different from GEMs used for other applications. Thus, our base material is of proven reliability and we know its properties well. Starting with this flat GEM foil we use a method similar to thermoplastic heat-forming; the foil is forced into a new shape by stretching it over a spherical mold, see Fig. 4.4. After a heat cycle it keeps this spherical shape.

Heat-forming

Heat-forming is routinely done with thermoplastic polymers, where above the so-called *glass transition temperature* monomers can migrate freely, and polymerize again upon cooling down. However the polyimide substrate of GEMs is a thermoset polymer which has no well-defined glass transition temperature. Strongly heating a polyimide leaves the polymer chains intact, but allows cross-links between chains to break or dislocate, thus relieving

mechanical stresses. Starting from a certain temperature the polyimide will start to degrade irreversibly; it becomes weak, brittle and dark-colored, see Fig. 4.5. This degradation is mainly caused by oxidation of the radicals that are exposed when these cross-links or polymer chains break. We found that 350° C is the highest temperature we can apply to our foils without damaging the quality of the polymer significantly. This limit can be increased to at least 400° C if the forming is performed in a vacuum of 10^{-4} mbar or better.

Figure 4.4 shows the simple setup designed for forming GEMs spherically. It consists of a spherical mold, a ring-and-plate structure to hold the foil to be formed, and four rods along which the plate can slide down toward the mold. Weights are applied to the plate to control the force that stretches the foil over the mold. Note that, contrary to thermoplastic heat-forming, the foil cannot be allowed to slip between the ring and plate where it is mounted. The degree to which monomers migrate during the forming is much less than for thermoplastics; foils that accidentally slipped during forming were consistently wrinkled. Also, the forming process for polyimide is apparently very slow: we found that the shortest heat cycle that gave satisfying results took 24 hours.

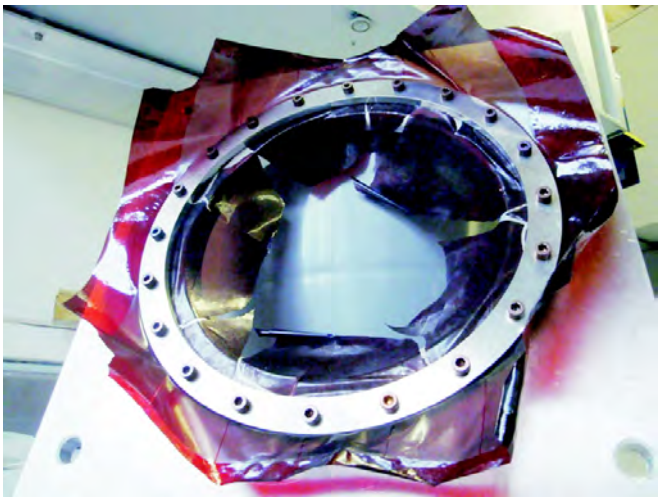

Figure 4.5 — The result of overheating a foil when trying to form it. The electrodes of this GEM were removed beforehand to avoid their oxidation. During the forming procedure it was heated up to 400° C.

Oxidation

Due to this long heating time and the high temperatures, the copper electrodes get fully oxidized in the process. From such deep oxidation, electrodes cannot be recovered by etching. The oxidation also causes some delamina-

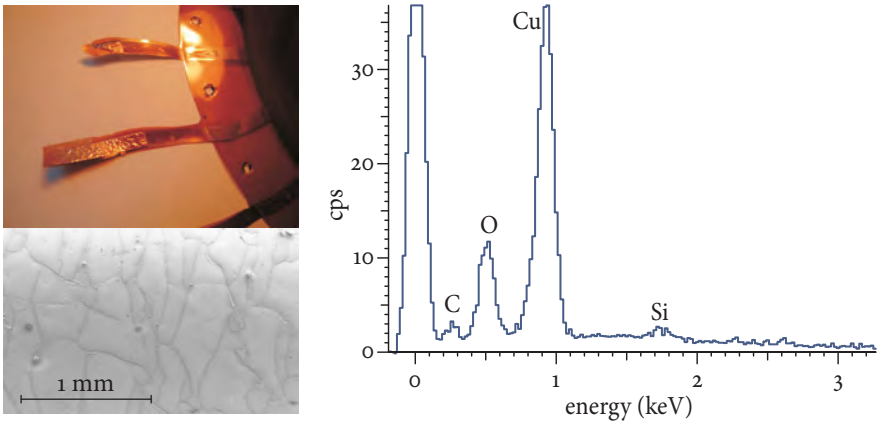

Figure 4.6 — Left: deposits on the electrode after heat-forming a GEM in an argon atmosphere. Right: result of an energy-dispersive x-ray spectroscopy (EDS) analysis of a sample of these deposits. The deposits consist only of copper oxide, the carbon and silicon peaks come from the adhesive used to move the deposit from the GEM to the EDS setup.

tion of copper from the polyimide substrate. Therefore the procedure should be carried out in an oxygen-free atmosphere.

Tests performed in a gas-tight enclosure with a constant flow of argon show that oxidation can indeed be largely avoided. However, after forming, the electrodes are covered with a thin film of a shiny substance, see Fig. 4.6. Elemental analysis of these deposits identifies the material as copper oxide, as shown in the plot on the right of figure 4.6. Apparently the argon atmosphere is not pure enough to avoid oxidation entirely. Moreover, such a loosely attached film develops from outgassing products which are not removed from the foil in the atmospheric pressure. These deposits can be removed afterwards, but as it involves mechanical brushing or rather strong water spraying this is likely to affect the spherical shape and should better be avoided.

Vacuum

To avoid formation of these deposits as much as possible the procedure should be carried out in a vacuum. To this end, the gas-tight vessel was upgraded with heat-resistant graphite gaskets to contain a vacuum of ultimately 10^{-4} mbar. Under these conditions, no more deposits were observed and the electrodes were hardly oxidized. The oxidation of the electrode facing the mold, however slight, left an image of the electrode on it. This thin copper oxide film turned out to be a useful anti-adhesive, and enabled us to remove GEMs from the mold without exerting any force. This was never possible with a newly polished mold.

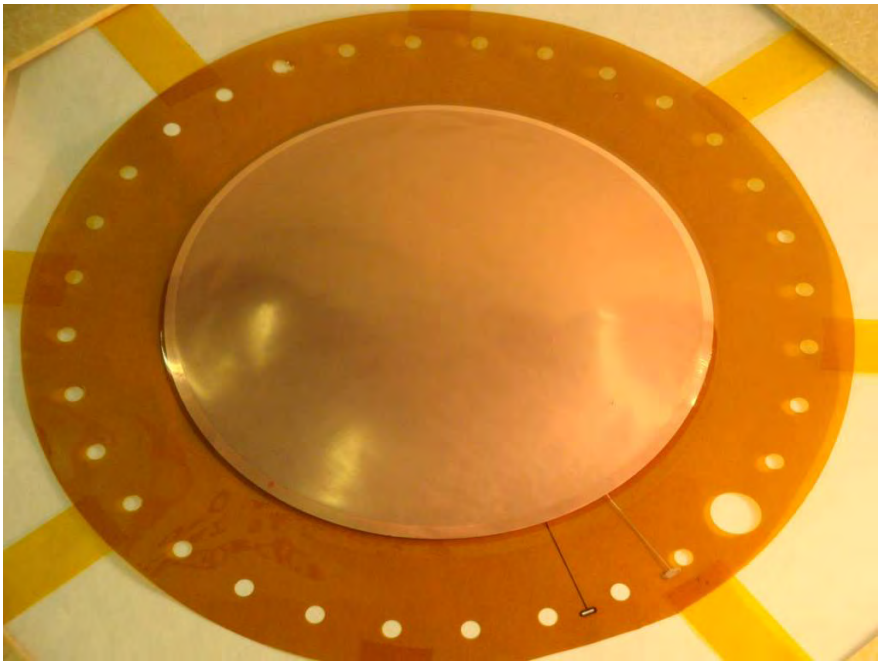

Figure 4.7 — Spherical GEM made in a vacuum of ~ 10^{-4} mbar.

An attractive side-effect of the lengthy heat cycle under vacuum is that the polyimide outgasses all unbound molecules present in its structure, and thus becomes an ultra-high vacuum compatible material. In [71] such a condition is reached after 10 hours in vacuum at a temperature of 150° C. From such clean materials one can build *sealed* detectors, in which the gas is not flowing. This opens the way to use more efficient gases such as xenon (see Fig. 4.1), which would otherwise be prohibitively expensive.

4.2.1 Resulting spherical GEMs

The spherical GEMs made in this manner normally have the same discharge voltage (in air: ≥600 V) and leakage current (~2 nA) as before the heat-forming treatment. Surprisingly, GEM holes observed through a microscope do not show any visible deformation, be it in the central area or closer to the edge. This suggests that stresses are spread evenly across the foil and not concentrated in certain regions.

Making this assumption, one can estimate the change in relevant dimensions due to spherical bending. The active area of the foil before (flat) and

after stretching (curved) is:

$$A_{\text{flat}} = \frac{\pi d^2}{4} = \pi r^2 \sin^2 \theta_{1/2}, \tag{4.1}$$

$$A_{\text{curved}} = 2\pi \int_0^{\theta_{1/2}} r^2 \sin\theta \mathrm{d}\theta = 2\pi r^2 \left(1 - \cos\theta_{1/2}\right). \tag{4.2}$$

Here r is the radius of curvature of the sphere, and $\theta_{1/2}$ is half the opening angle as indicated in figure 4.3. Then the surface stretching factor is:

$$\frac{A_{\text{curved}}}{A_{\text{flat}}} = 2\frac{1 - \cos\theta_{1/2}}{1 - \cos^2\theta_{1/2}}, \tag{4.3}$$

and depends only on the opening angle. If we substitute the opening angle from figure 4.3, we obtain 10.7% increase in area for the spherical GEM.

Increased capacitance

This stretching factor increases the capacitance between the electrodes of a foil, and this will also increase the power generated in a discharge. The area of the foil should increase with the stretching factor, the thickness of the dielectric should decrease with the same factor. Hence the capacitance is expected to increase with the square of the stretching factor: 23%. The increase in capacitance was measured on the few spherical GEMs made so far, and it was consistently lower than expected: 11%. This suggests that the holes may be more strained by the stretching tension than the material between the holes.

Another effect to be taken into account is the aspect ratio of GEM holes (defined as *depth/width* of a hole), which in turn influences the amplifying behavior of the GEM. The change in width of a hole is proportional to the square root of the stretching factor, and the change in depth is inversely proportional to the stretching factor. This results in an aspect ratio reduced to 86% with respect to te initial state. This is compensated in the design by changing the diameter and pitch of holes from the standard 140/70 microns to 120/60 microns. If it is true that holes are strained more than the material surrounding them, like suggested above, the aspect ratio may still be somewhat reduced.

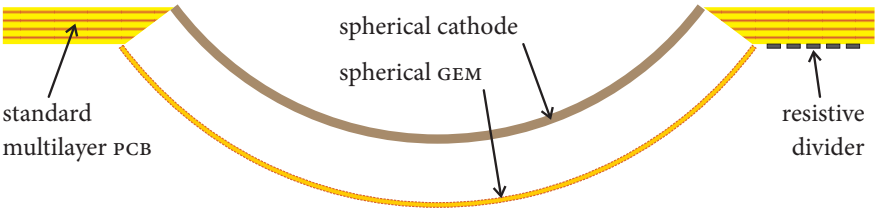

Figure 4.8 — The principle of a conical field cage made from a multilayer PCB.

4.2.2 *Conical field cage*

The field quality in the drift region is of critical importance, as the elimination of the parallax error depends on it. We designed a field cage to maintain a good radial field until the edge of the active area. This field cage is a conical enclosure of the conversion region, and is made from a standard multilayer PCB, see Fig. 4.8. The inner metal layers serve as field electrodes. A resistive divider defines the voltages supplied to each layer. It also serves as a rigid mechanical fixture to which the GEM can be glued, and as a high voltage distributor which supplies the GEM.

Field simulations done with the Ansys[1] field solver indicate that the thin field electrodes (compared to the relatively wide strips commonly used in time projection chambers) do not give rise to field spikes close to the field cage. Varying the thickness of the electrodes and the number of electrodes, the field distortions were simulated. Figure 4.9 shows that the fringes where field distortions are greater than 1% of the nominal field steadily decline with increasing number of electrodes, and with decreasing electrode thickness. The final prototype field cage we produced has 5 electrodes of ~40 µm thickness.

4.2.3 *Curved spacers*

Although spherical GEMs seem to be largely self-supporting, we developed curved spacers to add some rigidity and to tighten mechanical tolerances, see figure 4.10. Flat spacers can easily be machined from plate material, but curved spacers are challenging both to design and manufacture. We designed spacers to match our spherical GEMs with Catia[2] 3D design software.

Stereolithography

The manufacturing was done using a technique called stereolithography, often used in industry for rapid prototyping of small, complex-shaped objects. Objects are made out of a bath of liquid epoxy, which is selectively polymerized

[1] http://www.ansys.com/
[2] http://www.3ds.com/products/catia

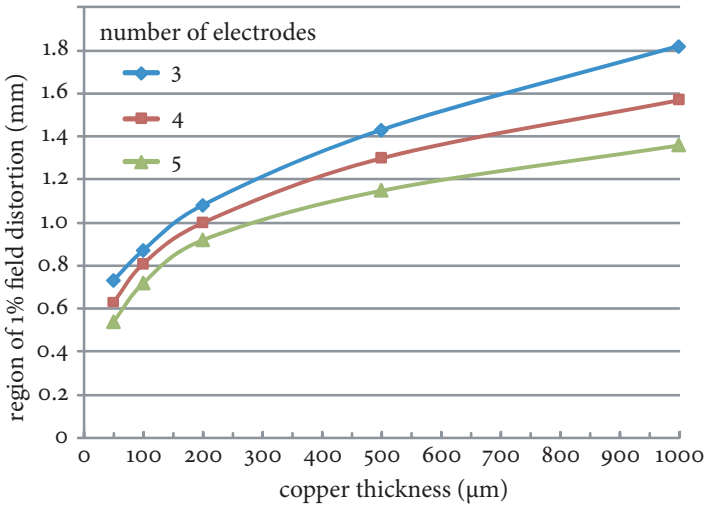

Figure 4.9 — Results of field simulations of a conical field cage. The width of the region with more than 1% field distortion is plotted versus the thickness of the copper layers in the PCB, for the case of 3, 4 and 5 electrodes in the field cage.

Figure 4.10 — A curved spacer made by stereolithography.

in a 2D pattern by a UV laser. By consecutively making a large stack of such 2D patterns, the object takes shape. The accuracy is often 100 µm or better in all three spatial coordinates. A number of liquid epoxies are suitable for this process, and one should choose the best in terms of rigidity, outgassing and dielectric strength.

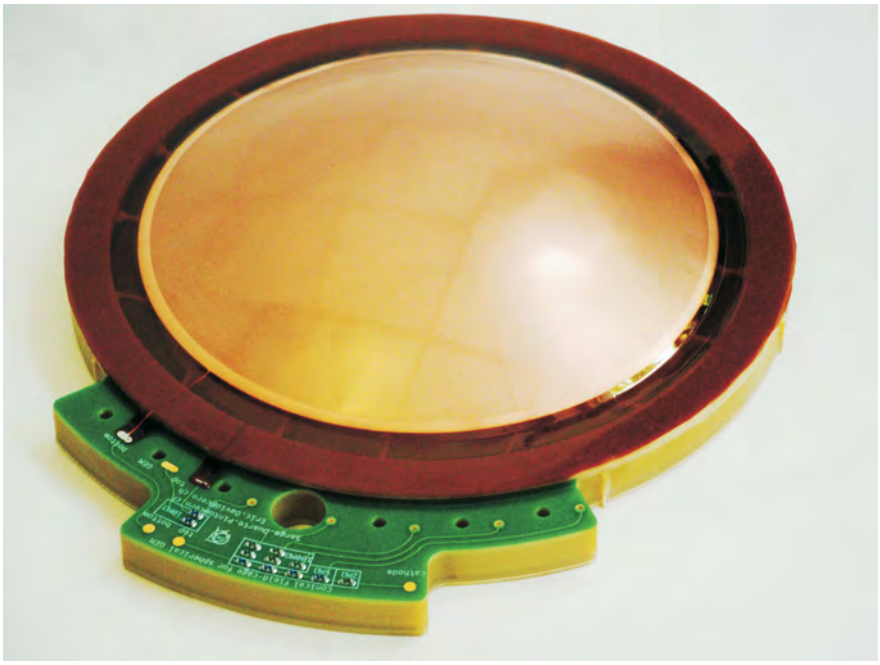

Figure 4.11 — An assembly of a spherical GEM, a conical field cage and a curved spacer.

4.3 First results

An assembly was made consisting of one spherical GEM, a conical field cage and a curved spacer, see Fig. 4.11. This assembly was mounted in the detector mentioned above, with a spherical beryllium entrance window. The detector needed some modifications in order to operate the GEM in it, and some hardware issues are not entirely solved at the time of writing. Therefore a full characterization of the properties has not yet been completed. However, using a pA-meter typical GEM behavior has been observed. Figure 4.12 shows the anode current as a function of voltage applied to the GEM. At low voltage the GEM becomes transparent to electrons coming from the conversion gap. The anode current then reaches a plateau at full transparency, and when the voltage is further increased multiplication starts. In the present conditions we report a gain up to 30; in general the spherical GEM seems likely to perform just like a standard GEM.

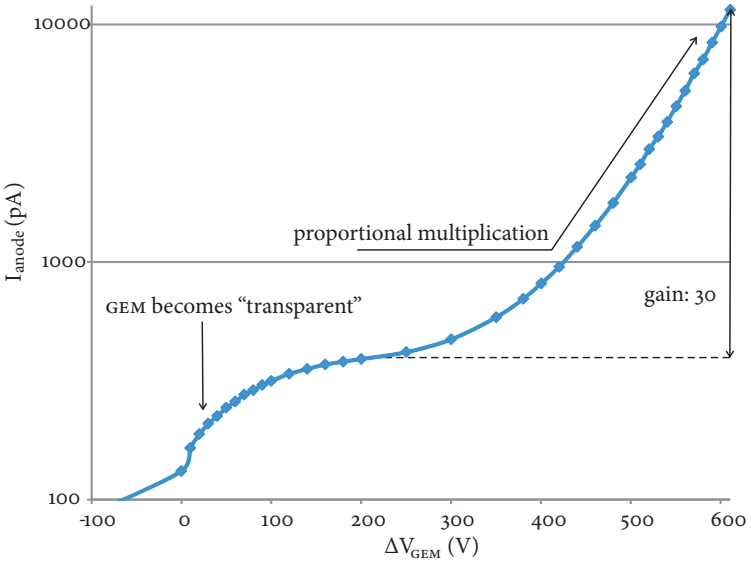

Figure 4.12 — Anode current of the setup shown in Fig. 4.3 versus voltage applied to the GEM. The gas mixture is Ar/CO_2 70%/30% at an absolute pressure of 2 bar. Hardware issues with the detector in which the spherical GEM assembly was installed kept us from raising the voltage further.

4.4 Further development

Now that the feasibility of making and operating spherical GEMs is demonstrated, we can start optimizing the readout structure. In the present setup with a flat readout structure, the electric field between the spherical GEM and the readout structure is rather non-uniform. This is shown in Fig. 4.13, where the field strength just below the GEM in Fig. 4.3 is plotted versus the angle with respect to the central axis. This field extracts electrons from the GEM holes, and influences the effective gain considerably. Also, signal induction times vary considerably from the center of this detector to the periphery due to longer drift paths, and the weaker field in the periphery aggravates this effect.

The most obvious solution that comes to mind is making the readout structure spherical as well. This is quite challenging, even now that we took the hurdle of making spherical GEMs. The most difficult step is the image transfer; no methods exist that allow transfer to spherical surfaces. This was also the main reason to make spherical GEMs from completely finished planar GEMs.

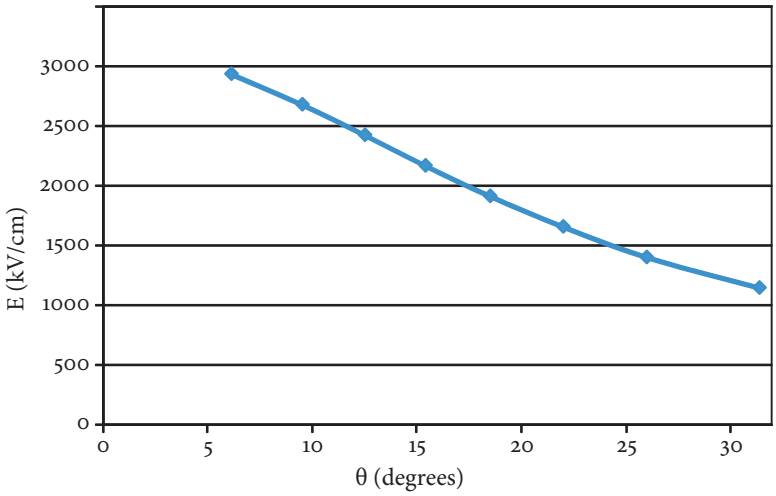

Figure 4.13 — Extraction field versus angle for the spherical GEM with planar readout of Fig. 4.3.

Therefore we foresee making a planar 2D readout circuit from the same base material as GEMs: copperclad polyimide. Such a readout circuit can be formed using the same tools and method as for spherical GEMs. There are still a few rather severe constraints, however. Any readout structure with more than two metal layers requires some sort of adhesive to make a multilayer board; no known adhesives are compatible with the temperatures used while forming. Even two metal layers can only be used if we can include vias in the structure; we have yet to prove that vias can survive the harsh heat-forming treatment.

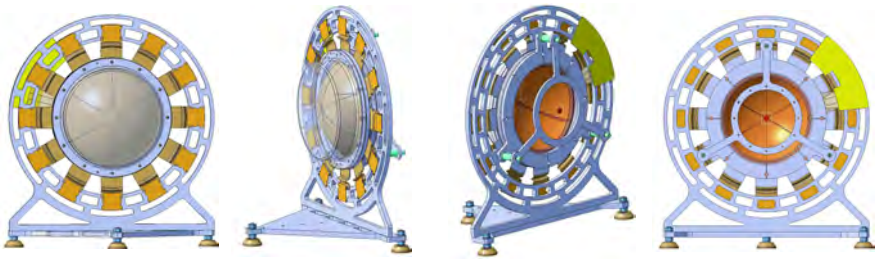

Figure 4.14 — 3D design of a spherical multiple GEM detector with spherical readout board from various points of view. The spherical active area has a diameter of ~ 17 cm, the whole structure is ~ 40 cm high.

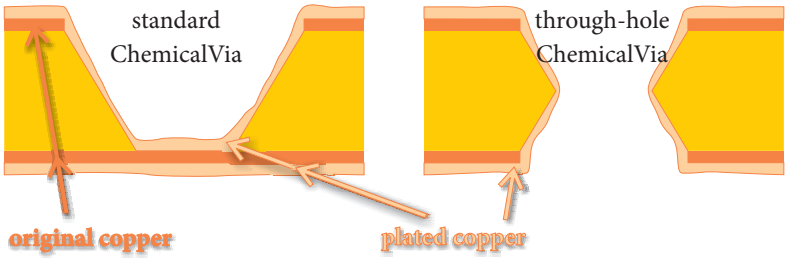

Figure 4.15 — Through-hole ChemicalVia (right) that is expected to survive a heat-forming treatment, contrary to standard ChemicalVias (left).

A microvia technology recently developed at CERN (based on the *ChemicalVia* technology developed earlier [72]) is expected to deliver vias that cannot be damaged by this treatment. In a standard *blind* ChemicalVia (see Fig. 4.15, on the left) the adhesion of the plated copper layer to the copper that was originally part of the base material is not very strong, and could break when stretching and heating. A *through-hole* version of such a via can be made by plating a "GEM-style" biconical hole; the contact between layers does not depend on the adhesion of the plated copper in this case. A preliminary design of an 2D θ-ϕ readout structure based on such vias (triplicated for redundancy) is made and ready for production. Figure 4.16 shows a simplified drawing of this readout structure, indicating how one coordinate is read out by radial strips of varying length on the top layer (shown in red), and the other coordinate by pads on the top layer that are interconnected by a circular trace on the bottom layer (blue). Also mechanical designs for an all-spherical gas detector are at an advanced stage, see Fig. 4.14.

4.5 Conclusions & outlook

We developed spherical GEMs, a conical field cage, and curved spacers, in order to make a parallax-free gas detector. A first assembly is installed in an existing detector, which provides a spherical beryllium entrance window and a flat 2D readout board. Familiar GEM behavior has been demonstrated, consistent with standard flat GEMs. The observed gain of up to 30 is expected to improve by one or two orders of magnitude when hardware issues with the detector are solved.

Plans have been made to develop also a spherical readout structure. We made designs and identified technologies to make such a circuit, and also the mechanical structures necessary to build an all-spherical detector.

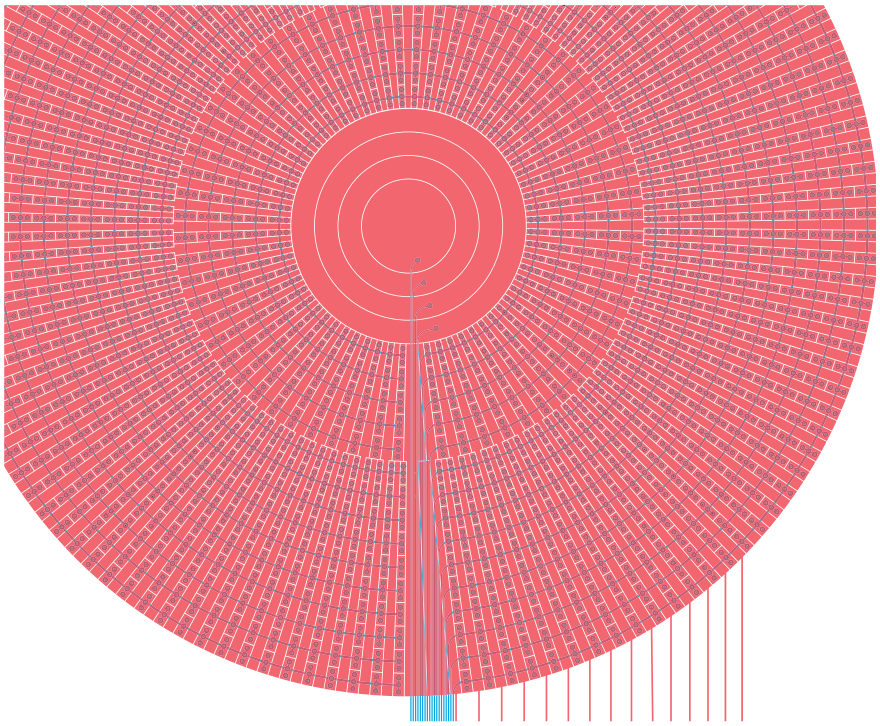

Figure 4.16 — A simplified design of a spherical readout structure. In red the metal on the top layer, transparent to reveal the bottom layer underneath in blue. The φ- and θ-coordinates are read out by strips and pads, respectively. The readout pads are interconnected by circular traces on the bottom layer. All vias are triplicated for redundancy.

Summary

The working principle of micropattern gas detectors (MPGDs) is similar to that of wire-chambers: proportional charge amplification by an electron avalanche caused by a strong electric field. Compared to wire-chambers MPGDs have much shorter distances between electrodes, so that charges in the chamber have shorter drift times before they are collected. Therefore MPGDs have fast, short signals, and a high rate-capability. Other common benefits compared to wire-chambers include a good energy, time and spatial resolution, natural suppression of ion and photon feedback, apparent resistance to aging, cost and ease of production. Despite their many advantages, MPGDs have some common issues such as discharges or the charging of dielectric surfaces. Many different micropattern technologies have been invented since the 1990s, and more are still being developed. One of the most prominent and generally successful of these technologies is the *gas electron multiplier* (GEM).

A GEM is a charge multiplication structure made from a copper clad polymer foil, pierced with a regular and dense pattern of holes. Like many MPGDs, GEMs are manufactured using techniques that are common in the industry of printed circuit boards: photolithography and chemical etching. As a GEM alone is only a charge amplification structure it is functionally independent from the readout structure, which leaves freedom to optimize the latter without restrictions. Also, the fact that electrons flow through the holes in the GEM foil and are then extracted by an electric field leaves the possibility to cascade GEMs. This is routinely done in applications demanding a high gain ($> 10^4$) with a negligible probability of discharging, and the triple GEM has become a de facto standard.

A triple GEM cascade needs 7 high voltages (the cathode and 3×2 GEM electrodes), and a uniform spacing between the electrodes in order to have a well-defined field in all the gaps. To this end, GEM foils are normally stretched and glued to stiff flat frames of well known thickness, after which these frames foils are stacked together with a cathode and a readout electrode to complete the chamber. The foils, frames and readout circuit must be carefully designed to avoid conflicts between high voltage distribution, gas routing and signal traces. Proper validation of a detector requires both lab tests to establish a gain calibration and measure discharge probability, and beam tests using the envisaged readout electronics to measure among others the efficiency for the detection of minimum ionizing particles.

Large area GEMs have applications primarily in high-energy and nuclear physics, in zones where high radiation fluxes are foreseen. There are many challenges in developing large area GEM detectors. Manufacturing large GEM

foils required an upgrade to the method with which GEMs were normally made. The introduction of a *single-mask technique* overcame the mask alignment issues that prohibited making GEMs longer than ~ 0.5 m in the past. This technique results in somewhat different hole shapes than before, and the performance needed to be validated. The engineering of the etching process to modify the hole shape resulted in an excellent control over all parameters and the symmetry of holes. To overcome the limited width of the available base material, I developed a splicing method in which foils are joined over a narrow seam. The bigger foil thus obtained can be stretched and framed like any simple foil, leaving only a slim dead region ($\sim 2mm$) under the seam. The single-mask technique and splicing method combined allow making foils of in principle any size. Other improvements made to accommodate large area GEMs concern the handling of GEMs during manufacturing and assembly, the distribution of high voltages and the stretching and framing of GEMs. Most of these methods and techniques are already adopted by LHC experiments and other efforts.

Spherical GEMs can be used to eliminate the *parallax error* in the detection of neutral radiation from a point-like source. This error is caused by the wide spread in conversion depth of these neutral particles in the gaseous medium. Although the benefits of giving a GEM a spherical shape was recognized long ago by its inventor, no attempt was previously made to realize this. I developed a method to make spherical GEMs, and demonstrated their performance. The method used involves rather extreme conditions, like high temperature, high mechanical tension and a high vacuum. Nevertheless, the resulting GEMs are not damaged, the hole pattern is not significantly deformed, and it holds high voltage. Along with the procedure for making spherical GEMs, I developed a conical field cage to maintain a good field quality until the edge of the foil, and curved spacers for mechanical stability and a proper spacing in case more GEMs are cascaded. The first working assembly of these components was successfully tested with a planar readout structure. I also made plans for the production of a spherical 2D readout board.

Bibliography

[1] K. Nakamura et al. (Particle Data Group), *The review of particle physics*> J. Phys. G 37, 075021, 2010.

[2] *Stopping Powers and Ranges for Protons and Alpha Particles.* ICRU report No. 49, 1993.

[3] W. Blum, W. Riegler and L. Rolandi, *Particle detection with drift chambers.* Springer-Verlag, 2008. ISBN: 978-3-540-76684-1. DOI (per chapter): 10.1007/978-3-540-76684-1_1 through 10.1007/978-3-540-76684-1_12.

[4] J. Kaminski, *Time projection chamber with triple GEM and pixel readout.* Presentation given at the MPGD2009 conference in Kolympari, Crete, Greece, 2009. http://candia.inp.demokritos.gr/mpgd2009/

[5] R. Bellazzini et al., *Gas pixel detectors for x-ray polarimetry applications.* Nucl. Instr. & Meth. A vol. 560, issue 2, 10 May 2006, pp. 425–434. DOI: 10.1016/j.nima.2006.01.046.

[6] A. Dianoux, G. Lander, *Neutron Data Booklet.* Institut Laue-Langevin, 2003. ISBN: 0-9704143-7-4.

[7] E.B. Wagner, F.J. Davies and G.S. Hurst, *Time-of-flight investigations of electron transport in some atomic and molecular gases.* J. Chem. Phys, vol. 47, 1967.

[8] S. Ramo, *Currents induced by electron motion.* Proceedings of the IRE, vol. 27, issue 9, pp. 584–585, September 1939.

[9] W. Riegler . Nucl. Instr. & Meth. A, vol. 535, issues 1–2, 11 December 2004, pp. 287-293, DOI: 10.1016/j.nima.2004.07.129.

[10] A. Oed, *Position-sensitive detector with microstrip anode for electron multiplication with gases.* Nucl. Instr. & Meth. A, vol. 263, 1988, pp. 351–359.

[11] A. Oed, *Properties of micro-strip gas chambers (MSGC) and recent developments.* Nucl. Instr. & Meth. A, vol. 367, 1995, pp. 34–40.

[12] F. Sauli, *GEM: A new concept for electron amplification in gas detectors.* Nucl. Instr. & Meth. A, vol. 386, issues 2–3, 21/2/1997, pp. 531–534.

[13] F. Sauli et al., *Discharge studies and prevention in the gas electron multiplier (GEM).* Nucl. Inst. & Meth. A, vol. 479, issues 2–3, 1/3/2002, pp. 294–308.

[14] F. Sauli et al., *Construction, test and commissioning of the triple-GEM tracking detector for COMPASS.* Nucl. Instr. & Meth. A, vol. 490, issues 1–2, 1 September 2002, pp. 177–203. DOI: 10.1016/S0168-9002(02)00910-5.

[15] S. Lami, G. Latino, E. Oliveri, L. Ropelewski, N. Turini, *A triple-GEM telescope for the TOTEM experiment.* Nucl. Phys. B — Proc. Suppl. vol. 172, October 2007, pp. 231–233. DOI: 10.1016/j.nuclphysbps.2007.08.055. ArXiv:physics/0611178v1.

[16] G. Bencivenni et al., *High-rate particle triggering with triple-GEM detector.* Nucl. Inst. & Meth. A vol. 518, issues 1–2, 2004, pp. 106–112.

[17] Y. Giomataris, Ph. Rebourgearda, J.P. Roberta and G. Charpak, *Micromegas: a high-granularity position-sensitive gaseous detector for high particle-flux environments.* Nucl. Instr. & Meth. A, vol. 376, issue 1, 21 June 1996, pp. 29–35.

[18] L.I. Shekhtman et al., *Performance of MSGC on electronically and ionically conductive substrata in various operational conditions.* Nucl. Instr. & Meth. A vol. 348, 1994, pp. 344-350.

[19] R. Bellazzini et al., *The WELL detector.* Nucl. Instr. & Meth. A vol. 423, issue 1, 21 February 1999, pp. 125–134.

[20] R. Bellazzini et al., *The micro-groove detector.* Nucl. Instr. & Meth. A vol. 424, issues 2–3, 21 March 1999, pp. 444–458.

[21] J.F.C.A. Veloso, J.M.F. dos Santos and C.A.N. Conde, *A proposed new microstructure for gas radiation detectors: The microhole and strip plate* Rev. Sci. Instrum. 71, 2000, p. 2371.

[22] A. Lyashenko et al., *Efficient ion blocking in gaseous detectors and its application to gas-avalanche photomultipliers sensitive in the visible-light range.* Nucl. Instr. & Meth. A vol. 598, issue 1, 1 January 2009, pp. 116–120, DOI: 10.1016/j.nima.2008.08.063.

[23] V. Peskov et al., *Detection of the primary scintillation light from dense Ar, Kr and Xe with novel photosensitive gaseous detectors.* Nucl. Instr. & Meth. A vol. 478, issues 1–2, 1 February 2002, pp. 377–383.

[24] R. Chechik, A. Breskin, C. Shalem and D. Mörmann, *Thick GEM-like hole multipliers: properties and possible applications.* Nucl. Instr. & Meth. A vol. 535, issues 1–2, 11 December 2004, pp. 303–308.

[25] A. di Mauro et al., *A new GEM-like imaging detector with electrodes coated with resistive layers.* IEEE-NSS 2006 Conference record, MP4-2.

[26] I. Giomataris et al., *Micromegas in a bulk.* Nucl. Instr. & Meth. A vol. 560, issue 2, 10 May 2006, pp. 405–408.

[27] J.E. Bateman, *The pin detector — a simple, robust, cheap and effective nuclear radiation detector.* Nucl. Instr. & Meth. A vol. 238, issues 2–3, 1 August 1985, pp. 524–532

[28] S.F. Biagi and T.J. Jones, *The microdot gas avalanche chamber: an investigation of new geometries.* Nucl. Instr. & Meth. A vol. 361, issues 1–2, 1 July 1995, pp. 72–76

[29] J. Timmermans et al., *An electron-multiplying 'Micromegas' grid made in silicon wafer post-processing technology.* Nucl. Instr. & Meth. A vol. 556, issue 2, 15 January 2006, pp. 490–494.

[30] S. Platchkov et al., *A large size Micromegas detector for the COMPASS experiment at CERN.* IEEE-NSS 2002 Conference Record.

[31] D. Attié, *TPC review.* Nucl. Instr. & Meth. A vol. 598, issue 1, 1 January 2009, pp. 89–93. DOI:10.1016/j.nima.2008.08.114

[32] I. Tserruya et al., *A hadron blind detector for the PHENIX experiment at RHIC.* Nucl. Instr. & Meth. A vol. 546, issue 3, 11 July 2005, pp. 466–480.

[33] G.C. Smith, *Gas-based detectors for synchrotron radiation.* Journal of synchrotron radiation, 2006, 13, 172–179.

[34] A.V. Belushkin, E.S. Kuzmin and V.N. Shvetsov, *Status of the FLNP project on neutron position-sensitive detectors.* Nucl. Instr. & Meth. A vol. 529, issues 1–3, 21 August 2004, pp. 249–253.

[35] M. Titov, *Radiation damage and long-term aging in gas detectors.* arXiv:physics/0403055v2 [physics.ins-det], March 2004.

[36] S. Duarte Pinto, *RD51, an R&D collaboration for micropattern gaseous detectors.* Proceedings of the XLVII international winter meeting on nuclear physics, Bormio, January 2009. arXiv:0907.2673 [physics.ins-det]

[37] S. Duarte Pinto et al., *A large area GEM detector.* IEEE-NSS 2008 conference record, pp. 1426–1432. DOI:10.1109/NSSMIC.2008.4774683

[38] G. Bencivenni and D. Domenici, *An ultra-light cylindrical GEM detector as inner tracker at KLOE-2* Nucl. Instr. & Meth. A vol. 581, issues 1–2, 21 October 2007, pp. 221–224.

[39] J. Ball et al., *Micromegas tracker project for CLAS12.* Nucl. Instr. & Meth. A, vol. 604, issues 1–2, pp. 53–55, 1 June 2009. DOI: 10.1016/J.NIMA.2009.01.047.

[40] M. Hohlmann et al., *GEANT4 simulation of a cosmic ray muon tomography system with micropattern gas detectors for the detection of high Z materials.* IEEE Trans. Nucl. Sci., vol. 56 (3), 2009. [physics.ins-det/0811.0187v1]

[41] S. Mukhopadhyay and N. Majumdar, *Use of triangular elements for nearly exact BEM solutions.* arXiv:0704.1563v1 [math.NA], April 2007.

[42] M. Capeans and C. Rembser, *The GIF++ gamma irradiation facility at CERN.* CERN white paper, http://cern.ch/WP7/WP7_DOCUMENTS.htm

[43] T. Zeuner, *The MSGC-GEM inner tracker for HERA-B.* Nucl. Instr. & Meth. A, vol. 446, issues 1–2, 11 May 2000, pp. 324–330. DOI:10.1016/S0168-9002(00)00042-5.

[44] M. Capeans, *Aging and materials: lessons for detectors and gas systems.* Nucl. Instr. & Meth. A, vol. 515, issues 1–2, 1 December 2003, pp. 73–88. DOI:10.1016/j.nima.2003.08.134.

[45] G. Castellano, J. Osán and J. Trincavelli, *Analytical model for the bremsstrahlung spectrum in the 0.25–20 keV photon energy range.* Spectrochimica Acta B vol. 59, pp. 313-319, 2004.

[46] *X-ray data booklet.* LBNL, University of California, September 2009. http://xdb.lbl.gov/

[47] LUMI-06 workshop website, includes links to Indico pages and proceedings: http://care-hhh.web.cern.ch/CARE-HHH/LUMI-06/

[48] The TOTEM collaboration, *The TOTEM experiment at the CERN Large Hadron Collider.* 2008 JINST 3 S08007.

[49] L. Shektman et al., *Light multi-GEM detector for high-resolution tracking systems.* Nucl. Inst. & Meth. A, vol. 556, issue 2, 15/1/2006, pp. 495–497.

[50] F. Sauli, patent: *Radiation detector of very high performance and planispherical parallax-free x-ray imager comprising such a radiation detector.* WIPO WO/1999/021211.

[51] S. Duarte Pinto and R. de Oliveira, patent: *A method of manufacturing a gas electron multiplier.* WIPO WO/2009/127220. Describes the single-mask technique for making GEMs.

[52] M. Bordessoule et al., *A simplified read out for high-resolution linear gas detector.* Nucl. Inst. & Meth. A, vol. 390, issues 1–2, 1 May 1997, pp. 79–85.

[53] J.-C. Santiard et al., *Gasplex, a low-noise analogue signal processor for read out of gaseous detectors.* CERN ECP/94–17, 1994.

[54] E. Oliveri and E. Graverini, Beam test results presented during an RD51 collaboration meeting, Bari, 9/10/2010, http://indico.cern.ch/contributionDisplay.py?sessionId=4&contribId=75&confId=102799.

[55] D. Domenici et al., *Activity of CERN and LNF groups on large area GEM detectors.* Nucl. Inst. & Meth. A, vol. 617, issues 1–3, May 2010, pp. 151-154. DOI:10.1016/j.nima.2009.06.063

[56] J. Yu et al., *Development of GEM based digital hadron calorimeter.* IEEE-NSS 2008 conference record, pp. 1544–1548. DOI: 10.1109/NSSMIC.2008.4774703

[57] M. Tytgat et al., *Characterization of GEM detectors for application in the CMS muon detection system.* IEEE-NSS 2010 Conference Record. arXiv:1012.3675v1 [physics.ins-det]

[58] E. Storm and H.I. Israel, *Photon cross sections from 1 keV to 100 MeV for elements Z=1 to Z=100.* Nuclear Data Tables, A 7, 1970, 565–681.

[59] G. Charpak, *Parallax-free, high-accuracy gaseous detectors for x-ray and VUV localization.* Nucl. Inst. & Meth. 201, 1982, pp. 181–192.

[60] J.K. Black et al., *The imaging x-ray detector for Lobster-ISS.* Nucl. Inst. & Meth. A, vol. 513, 2003, pp. 123–126.

[61] Z. Hajduk, G. Charpak, A. Jeavons, R. Stubbs, *The spherical drift chamber for x-ray imaging applications.* Nucl. Inst. & Meth. I 22, 1974, pp. 307–312.

[62] P.F. Christie, E. Mathieson and K.D. Evans, *An x-ray imaging proportional chamber incorporating a radial field drift chamber.* Journal of Physics E: Scientific Instruments, vol. 9, 1976, pp. 673–676.

[63] S.P. Chernenko et al., *Test results of the parallax-free x-ray area detector CD-1000 in the diffractometer CARD-7.* Nucl. Inst. & Meth. A, vol. 367, 1995, pp. 76–78.

[64] Y. Diawara et al., *A parallel-plate resistive-anode gaseous detector for x-ray imaging.* IEEE transactions on nuclear science, vol. 51, June 2004.

[65] P. Rehak, G.C. Smith, B.Yu, *a method for reduction of parallax broadening in gas-based position sensitive detectors.* IEEE transactions on nuclear science, Vol. 44, June 1997.

[66] B. Guérard et al., *Advances in detectors for single crystal neutron diffraction.* Nucl. Inst. & Meth. A, vol. 554, 2005, pp. 392–405.

[67] S. Duarte Pinto et al., *Making spherical GEMs.* 2009 JINST 4 P12006. DOI: 10.1088/1748-0221/4/12/P12006.

[68] S. Duarte Pinto et al., *Spherical GEMs for parallax-free detectors.* IEEE Nuclear Science Symposium 2009 Conference Record pp. 225–230. DOI: 10.1109/NSSMIC.2009.5401786.

[69] S. Duarte Pinto et al., *First results of spherical GEMs.* IEEE Nuclear Science Symposium 2010 Conference Record. arXiv:1011.5528v1 [physics.ins-det].

[70] K. Kurvinen et al., *Outgassing analysis of various detector materials.* IEEE-NSS 2003 conference record, vol. 5, pp. 3726–3730. DOI:10.1109/NSSMIC.2003.1352716.

[71] K. Kurvinen et al., *Gem detectors for x-ray astronomy.* Nucl. Instr. & Meth. A, vol. 513, issues 1–2, 1 November 2003, pp. 155–158. Doi:10.1016/j.nima.2003.08.022.

[72] R. de Oliveira et al., *An innovative* ChemicalVia *process for the production of high density interconnect printed circuit boards.* Circuit World vol. 30, iss. 4, pp. 27–33. Doi: 10.1108/03056120410539885.